Unraveling the Detection Mechanism of Indium Oxide Based Gas Sensors

Dissertation
der Mathematisch-Naturwissenschaftlichen Fakultät
der Eberhard Karls Universität Tübingen
zur Erlangung des Grades eines
Doktors der Naturwissenschaften
(Dr. rer. nat.)

vorgelegt von
Inci Boehme geb. Can
aus Albstadt-Ebingen

Tübingen
2020

Gedruckt mit Genehmigung der Mathematisch-Naturwissenschaftlichen Fakultät der Eberhard Karls Universität Tübingen.

Tag der mündlichen Qualifikation:	07.10.2020
Stellvertretender Dekan:	Prof. Dr. József Fortágh
1. Berichterstatter:	Prof. Dr. Udo Weimar
2. Berichterstatter:	Prof. Dr. Reinhold Fink

Contents

List of Abbreviations

at%	atom percentage
a.u.	arbitrary unit
BSE	backscattered electrons
DC	direct current
DFPT	density-functional perturbation theory
DFT	density functional theory
DRIFTS	diffuse reflectance infrared Fourier transform spectroscopy
e.g.	lat.: exempli gratia - engl. for example
et al.	et alia
etc.	et cetera
FTIR	Fourier-transform infrared
FWHM	full width at half maximum
GGA	generalized gradient approximation
GMS	gas mixing system
ICSD	Inorganic Crystal Structure Database
ip	in-plane
IR	infrared
ITO	indium tin oxide
LAAS	Laboratoire d'Analyse et d'Architecture des Systèmes
LCD	liquid crystal display
MCT	mercury cadmium telluride
MFC	mass flow controller
NEB	nudged elastic band
OLED	organic light emitting diode
oop	out-of-plane
PAW	projector-augmented wave
pH	power of hydrogen
RH	relative humidity
RT	room temperature
SEM	scanning electron microscopy
SMOX	semiconducting metal oxide
STM	scanning tunneling microscop
syn. air	synthetic air
UHV	ultra-high vacuum
VASP	Vienna Ab initio Simulation Package
VMD	Visual Molecular Dynamics
VOCs	volatile organic compounds
XPS	X-ray photoelectron spectroscopy
XRD	X-ray diffraction

List of Symbols

A	absorbance
Å	angstrom
$b_{1/2}$	the line broadening at half the maximum intensity
°C	degree Celsius
cm	centimeter
E	energy
eV	electronvolt
g	gram
h	hour
kV	kilovolt
λ	wavelength
m	mass
mbar	millibar
ml	milliliter
min	minute
mV	millivolt
n	amount of substance
nm	nanometer
Ω	ohm
ppm	parts per million
R	resistance
S	sensor signal
SC	single channel spectrum
T	time
τ	average crystal size
θ	Bragg angle
V	volt or vacancy
$\widetilde{\nu}$	wavenumber
W	watt

1

Introduction

When the German chemists Ferdinand Reich and Theodor Richter discovered indium in 1863, they could not know the future significance of this element for the technical world. Named after its color indigo in the absorbance spectrum, indium has been used in numerous application areas ranging from anticorrosive coatings to semiconductor-related technologies [1, 2]. In most compounds, this element has the +3 oxidation state [3]. Indium (III) oxide is a widely used compound which is an n-type semiconductor with several interesting characteristics. Especially the ternary composition indium tin oxide (ITO) is an important transparent material for liquid crystal displays (LCDs) [4], in solar cells [5] or in organic light emitting diodes (OLEDs) [6]. Additionally, the ability of In_2O_3 to change its resistance during the exposure to target gases or vapors, makes it an outstanding semiconducting metal oxide (SMOX) gas sensing material [7].

The applicability of semiconductors as gas sensing materials was first indicated by the discovery of the gas sensitive properties of germanium in 1953 [8]. One year later, Heiland reported the conductivity change of ZnO, the first SMOX, under gas exposure [9]. In 1962, N. Taguchi patented the first commercially available SnO_2 gas sensor [10] and the focus has remained largely on this material ever since. Today, SnO_2 is the most-investigated and thus the best-understood material used for SMOX based gas sensors [11].

SMOX gas sensors have many advantages like high stability, sensitivity and they can be miniaturized lowering power consumption [12]. Selectivity, however, is one of the main challenges in this field, which limits the usage of SMOX gas sensors dramatically. Combination of different SMOX materials with different gas responses and properties into sensor arrays is one possible way to address this problem.

In_2O_3 is a less investigated material [13] which shows interesting properties different from those of SnO_2 [14]. In addition, it responds well to CO, methane and volatile organic compounds (VOCs) [7, 15–19]. One of the greatest advantages of In_2O_3 is its ability to detect oxidizing gases like O_3, NO_2 or Cl_2 selectively at low temperatures [20–23]. It has been shown that by varying surface area, morphology, operation temperature or adding dopants/loadings, the gas sensing properties can be changed completely [11, 24, 25]. By understanding the sensing properties of In_2O_3, in the future, the performance could be controlled and fine-tuned. The following section gives a review of the most important findings over the last years which contributed significantly to the understanding of this material.

1.1 Literature Review

Generally, the sensing mechanism of SMOX gas sensors can be explained by the interaction of target gases or vapors with pre-adsorbed oxygen on the surface [11]. Yet, in recent years, there have been spectroscopic investigations and density functional theory (DFT) calculations showing a different nature of In_2O_3 compared to standard materials like SnO_2 or WO_3.

One of the few spectroscopic investigations on In_2O_3 was performed in 2013 by Sänze et al. using operando Raman/Fourier-transform infrared (FTIR) spectroscopy. The measurements were performed at 190 °C and 325 °C under exposure of 250 ppm ethanol in nitrogen and in synthetic air (syn. air). They were able to observe changes in the sensor properties which were related to surface oxidation states. In their proposed mechanism, ethanol adsorbed as acetate (2937 cm^{-1}) through the reaction with surface hydroxyl groups (3643 and 3659 cm^{-1}) leading to a decrease of the resistance of indium oxide. This indicated the formation of oxygen vacancies near the surface of In_2O_3. The observation of the Raman band at 2868 cm^{-1} and CO_2 (2361 cm^{-1}) in gas phase by IR-spectroscopy implied the decomposition of acetate to CO_2 by reacting with co-adsorbed oxygen via format-like species. The authors concluded that the mechanism strongly depended on conditions such as gas environment and temperature. They could show that the change in the resistance was related to three factors: nature of adsorbates, hydroxyl groups and indium oxide oxidation states. They excluded a sensing mechanism which was based only on formation/ionization and refilling of oxygen vacancies [26].

In addition to Raman spectroscopy, diffuse reflectance infrared Fourier transform spectroscopy (DRIFTS) was carried out. Under ethanol exposure in both syn. air and in nitrogen, bands at 1344, 1442 and 1575 cm^{-1} could be observed which were attributed to acetate groups. The increase of the C-H band at 2938 cm^{-1} and the simultaneous decrease of the surface hydroxyl groups at 3641 and 3657 cm^{-1} during the exposure to ethanol supported the reaction mechanism proposed based on the Raman experiments [27].

The effect of NO_2 exposure at different temperatures was investigated by Roso et al. via operando-DRIFT spectroscopy. The experiments revealed that the adsorption of NO_2 was the origin of the resistance change. However, depending on the temperature, the nature of the surface was different. At lower temperature (130 °C) the high amount of hydroxyl groups on the surface of In_2O_3 appeared to be beneficial for the adsorption of a large amount of NO_2 molecules and as a result the resistance changed significantly. Under NO_2 exposure, several bands in the IR-spectra could be observed. The band centered at 1221 cm^{-1} could be assigned to a nitrite ($NO_2{}^-$) species, whereas the ones at 1313 and 1260 cm^{-1} corresponded to nitrate ($NO_3{}^-$) species. The one centered at 1520 cm^{-1} could be both a nitrite or a nitrate. There was a clear correlation between the two surface species and the change in the resistance: while nitrite species were responsible for the resistance change, the nitrate species accumulated over time and consequently deactivated the surface for NO_2 sorption. As a result, the change in the resistance was lowered. At higher temperature (350 °C), less hydroxyl groups overall were present, and the terminal ones were more prominent. The reaction from nitrites to nitrates was dominant, and thus the changes in the resistance were limited [28].

Even though the results from both Sänze et al. and Roso et al. have contributed significantly to the understanding of In_2O_3 by showing how important the nature of the surface is and how it changes at different temperatures, the examination of only one material and the lack of information about water vapor make it difficult to generalize their findings. Humidity is prevalent in every application making it to the most significant interfering analyte [29]. The role of water vapor on In_2O_3 was examined by Wagner et al. using scanning tunneling microscopy (STM), X-ray photoelectron spectroscopy (XPS) and DFT studies on the (111) surface. Based on this investigation it was found that, three H_2O molecules could adsorb and dissociate on three symmetrically equivalent adsorption sites of the super cell forming each two hydroxyl groups. The surface was saturated once all adsorption sites were occupied which limited the maximal degree of surface hydroxylation. They also found, that the reactivity of the 3-fold coordinated lattice oxygen increased with the number of 6-fold coordinated In atoms in their direct neighborhood [30]. The results from Wagner et al. are significant and provide insights about the mechanism of water vapor on the surface of $In_2O_3(111)$. Formed hydroxyl groups were found to block the reactive dissociation sites and their overall surface adsorption was limited. However, there are major drawbacks to adopting their findings for gas sensors: the STM and XPS measurements were done at room temperature and in ultra-high vacuum (UHV), but SMOX gas sensors are generally operated at other conditions (e.g. normal pressure, operation temperature between 150 and 300 °C, etc.).

1.2 Scope of the Work

The knowledge of In_2O_3 gas sensors is based on very limited data. Although this oxide has been investigated over the last few decades, the sensing characteristics and the ongoing reaction mechanisms have not been dealt with in depth.

The aim of this work is thus to provide a complete picture of CO sensing and the influence of humidity with different In_2O_3 based sensors. The investigation methods are direct current (DC) resistance measurements of the sensing performance, DRIFT spectroscopy performed in *in-situ*/operando conditions and, additionally, DFT calculations to understand the empirically gained results. The aim is to identify variations in the reaction mechanism of this oxide depending on the synthesis route. CO was selected as target gas due to its high toxicity and because of its simple molecular structure. Its simple chemistry makes it an ideal candidate for a preliminary investigation. Humidity was introduced in this work because of its prevalence in most applications.

Additionally, oxidized noble metal clusters and their impact on the gas sensing will be investigated. Using additives is a common way to fine-tune the sensing properties. There is a large amount of work which has been done in recent years to understand their role during gas sensing. More knowledge about how they change the sensing properties could help to change the sensor characteristics in a controlled manner. DC resistance measurements in combination with DRIFTS investigation shall show first insights into the reaction mechanism.

2

Experimental and Theoretical Methods

Two different In_2O_3 powders were synthesized, labeled IC1 and IC2, in order to investigate and compare their sensing characteristics with commercially available In_2O_3 (Sigma-Aldrich, 99.98 % trace metals basis), labeled SA. Additionally, the commercially available powder was loaded with two different kinds of noble metal oxide clusters to investigate their effect on the sensing performance.

2.1 Material Synthesis

Synthesis of IC1

IC1 was obtained according to the synthesis route in [31]: $In(NO_3)_3 \cdot 5\,H_2O$ (Sigma-Aldrich, 99.99 %, trace metals basis) was added to 1 equivalent ammonium bicarbonate and ground for 30 minutes. The mixture was dried at 100 °C for 5 h and afterwards at 400 °C for 3 h to get In_2O_3 as a yellow solid.

Synthesis of IC2

IC2 was synthesized as described in [32,33]: By heating up $In(CH_3COO)_3$ (Sigma-Aldrich, 99.99 %, trace metals basis) to 400 °C for 3 h In_2O_3 was obtained as a yellow powder.

Synthesis of Noble Metal Loaded In_2O_3

The noble metal loading of SA In_2O_3 was done the same way as reported in [34]: In_2O_3 (Sigma-Aldrich, 99.98 %, trace metals basis) and $MCl_y \cdot xH_2O$ (Sigma-Aldrich, 99.98 %, trace metals basis) were stirred in 15 ml deionized water at a pH value of 1 by adding some drops of HCl at 80 °C for two hours and dried at

80 °C over night. The powders were grounded and afterwards calcined at 500 °C for 1 h. In order to ensure comparability and that the findings are not caused by the preparation route but by surface loading, the pure In_2O_3 was suspended in deionized water at a pH value of 1, stirred at 80 °C for two hours, dried at 80 °C over night and calcined at 500 °C for 1 h [35, 36]. The degree of loading of the produced powders was calculated using the following equation:

$$\text{at\%} = \frac{n(\mathrm{MCl_y \cdot xH_2O})}{n(\mathrm{In_2O_3})} \tag{2.1}$$

A list of the synthesized powders is shown in Table 2.1.

Table 2.1 List of the synthesized powders.

Sensor name	$m(\mathrm{In_2O_3})$ / g	$\mathrm{MCl_y \cdot xH_2O}$	$m(\mathrm{MCl_y \cdot xH_2O})$ / g
0.5 at% Rh-loaded In_2O_3	1.47	$\mathrm{RhCl_3 \cdot xH_2O}$	0.0055
1.0 at% Rh-loaded In_2O_3	1.50	$\mathrm{RhCl_3 \cdot xH_2O}$	0.0113
1.0 at% Pt-loaded In_2O_3	0.50	$\mathrm{PtCl_4 \cdot xH_2O}$	0.0610
pure In_2O_3	1.50	-	-

2.2 Sensor Preparation

The sensitive layers were deposited on Al_2O_3 substrates by screen printing: a printable paste was prepared by adding some drops of 1,2-propanediol (Sigma-Aldrich, 99.5+ % A.C.S. reagent) to each powder. The mixture was ground until a homogeneous paste was obtained. The paste was applied onto Al_2O_3 substrates using an Ekra Microtronic II screen printing device. This process is represented in Figure 2.1.

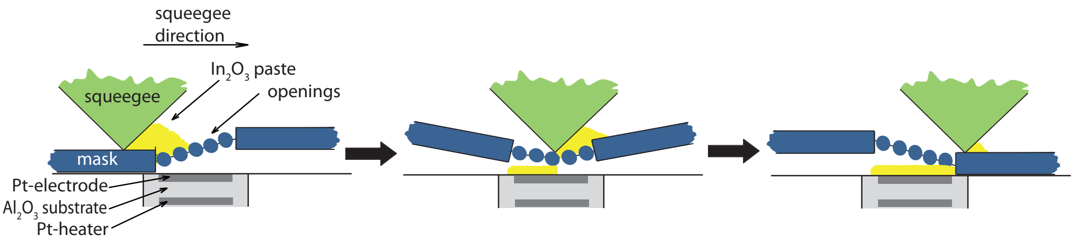

Figure 2.1 Sketch of the screen printing process. Adapted from [37].

The sensors were left at room temperature over night and afterwards dried in a Heraeus UT12 oven at 68 °C for 4 h. In a final step, the sensors were annealed in the Heraeus ROK 6/30 tube furnace at 400-500-400 °C, each 10 minutes to

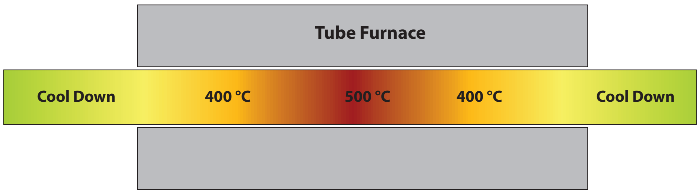

Figure 2.2 Temperature steps in the annealing procedure.

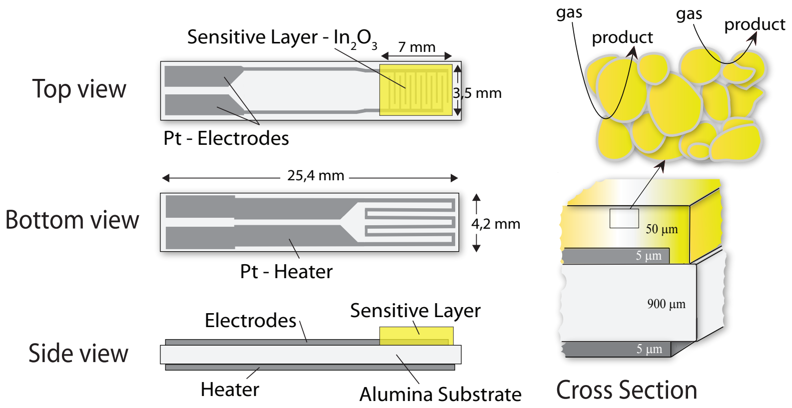

Figure 2.3 Schematic representation of a sensor's geometry from top/bottom/side view and cross section. Adapted from [37].

fully remove residual organic binders. An illustration of the calcination procedure is shown in Figure 2.2. A schematic representation of a typical screen printed sensor is shown in Figure 2.3. It consists of a sensitive layer with interdigitated platinum electrodes on the top and a platinum heater on the backside of the Al_2O_3 substrate.

The desired operation temperature of each sensor was controlled by applying a certain voltage to the platinum heater. The resistance of the Pt-heater is linear to the temperature. As the temperature-resistance correlation is different for each sensor, each sensor was calibrated. The voltage was increased from 2.0 V to 8.0 V in 1.0 V steps. At the same time the resistance of the platinum heater was read out and the temperature of the sensing layer was measured with an infrared pyrometer MAURER KTR 2300. A linear relationship is obtained by plotting the temperature against the resistance. An illustration of the calibration setup and an exemplary calibration curve is shown in Figure 2.4.

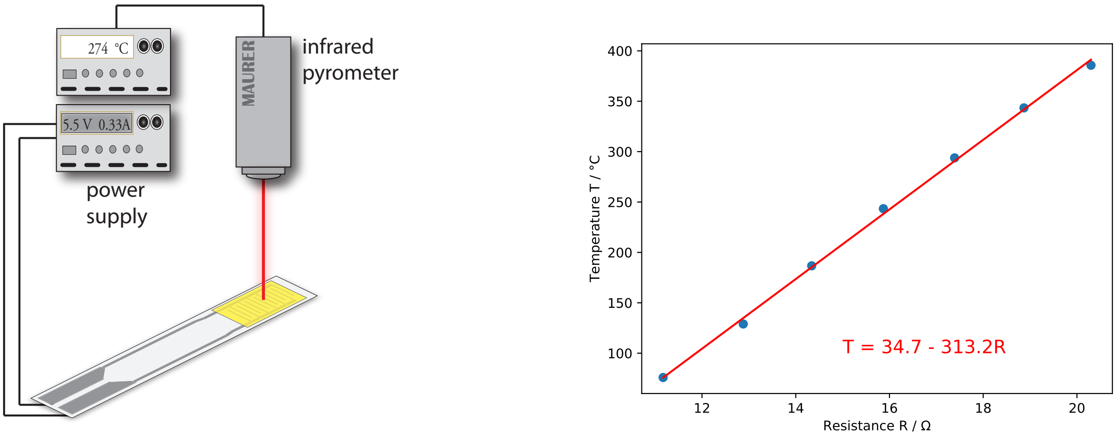

(a) Calibration setup with an infrared thermometer [38].

(b) Example of a calibration curve and the corresponding equation.

Figure 2.4 Calibration setup of the sensors for the operation temperature adjustment.

2.3 Material Characterization

To assess morphological and structural information, X-ray diffraction (XRD), scanning electron microscopy (SEM), and XPS measurements were performed. The XRD patterns of the sensitive layers were collected with a Philips X'Pert equipped with a monochromatic Cu K_α radiation source ($\lambda = 1.5405980$ Å). The diffraction spectra were taken from a 2 θ-ω angle of 10 to 70. The step size was 0.01 ° at a rate of 1 $^\circ/s$.

The SEM images were acquired with a HITACHI SU8030 cold field emission scanning electron microscope using an acceleration voltage of 3.0/5.0 kV. All SEM pictures were taken from the sensitive layer of the gas sensors.

The XPS measurements were done on the powders, pretreated identically to the sensor fabrication. The measurements were done in UHV conditions which was $< 10^{-9}$ mbar. The instrument was equipped with a hemispheric analyzer EA 125 (Omicron) and a conventional X-ray tube with 300 W. The spectra were recorded with a Mg K_α radiation of 1253.6 eV. For the detailed spectra a pass energy of 20 eV was used. All spectra were taken at normal emission using the high magnification lens mode. The XPS peak fitting of the spectra was performed using UNIFIT 2017.

2.4 DC Resistance Measurements

Measuring the DC resistance of the sensitive layer under gas exposure is a common approach to rate the sensing performance of SMOX gas sensors. The sensors were fixed in a socket with a feedthrough in an in-house made Teflon measurement chamber. To measure the resistance of the sensitive layer and control the operation temperature, the Pt-electrodes and the heater of the sensors were connected to a 34972A Agilent multimeter and E3614A voltage source, respectively. The desired composition of the gas mixture during the measurement was obtained by a computer controlled gas mixing system (GMS) and the in-house software mass flow controller (MFC). The sensors were measured at 300 °C. A typical setup is illustrated in Figure 2.5.

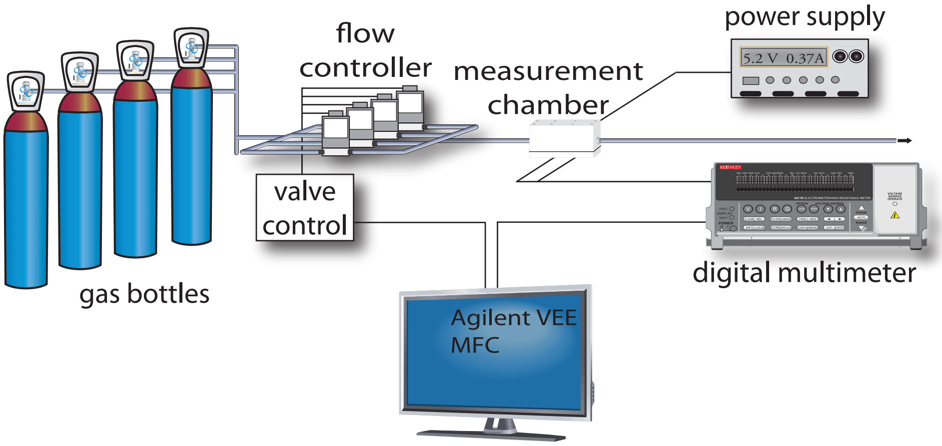

Figure 2.5 Setup of the DC resistance measurements. Adapted from [38].

The sensor signal S for reducing gases was calculated by dividing the resistance in syn. air ($R_{syn.\ air}$) by the resistance under exposure ($R_{reducing\ gas}$):

$$S = \frac{R_{syn.\ air}}{R_{reducing\ gas}} \tag{2.2}$$

The inverse relationship was applied to calculate the sensor signals of oxidizing gases.

2.5 DRIFT Spectroscopy

DRIFT spectroscopy is a powerful tool for the investigation of surface species. If the measurement is done *in-situ*/operando, insights into the surface reactions can be gained. The *in-situ*/operando DRIFTS measurements in this work were performed on a Bruker Vertex 70v and a Bruker Vertex 80v FTIR spectrometer, which are equipped with the Praying Mantis optic from Harrick. This optic ensures that mainly diffuse reflected light reaches the narrow-band mercury cadmium telluride MCT detector. The detector was cooled with liquid nitrogen. The sensors were fixed in a socket with a feedthrough in an in-house made measurement chamber containing a KBr window. The sensor was heated to the desired operation temperature. Simultaneously the DC resistance was recorded as described above. The spectrometers were evacuated whereas the sample compartment was kept at normal pressure. The single channel spectra were recorded every 15 min with a resolution of 4 cm^{-1} and 1024 sample scans using the software OPUS. An illustration of the setup is shown in Figure 2.6.

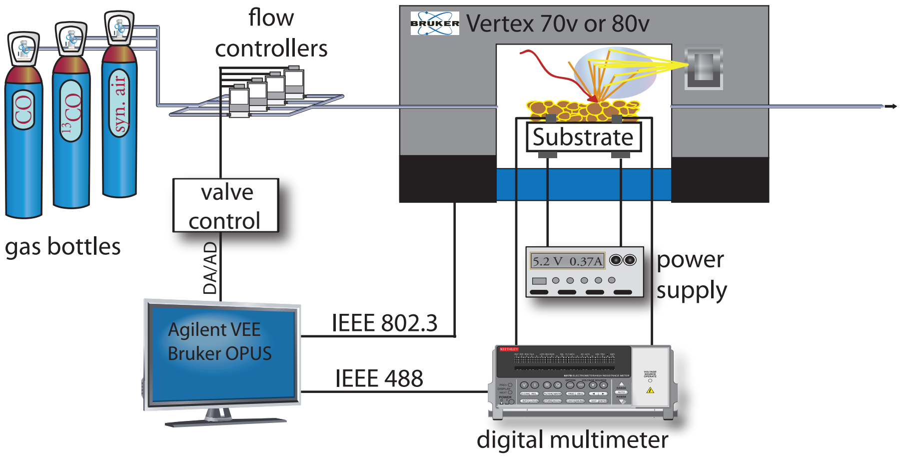

Figure 2.6 Setup of the DRFITS measurements. Adapted from [38].

To obtain valuable information about changes on the surface during gas sensing, isotopic labeled gases/vapors were used. The mass difference leads to characteristic shifts in the spectra, which enables the unambiguous identification of surface groups. In order to get the absorbance spectra, the relation suggested by Olinger and Griffiths was used [39]:

$$A = -\log\left(\frac{SC_{analyte\ gas}}{SC_{carrier\ gas}}\right) \tag{2.3}$$

where A represents the absorbance, $SC_{analyte\ gas}$ the single channel spectrum under analyte exposure and $SC_{carrier\ gas}$ the single channel spectrum gained under carrier gas. Increasing bands in the spectra indicate the formation of surface species/groups whereas decreasing bands indicate their cancellation.

2.6 DFT Calculations

DFT calculations are a valuable tool for modelling and understanding empirically gained information. The periodic DFT calculations in this work were performed using the plane wave program Vienna Ab initio Simulation Package (VASP). The geometries were optimized with the implemented Perdew–Burke–Ernzerhof exchange-correlation functional which belongs to the class of generalized gradient approximations (GGA). For the core electron representation, the projector-augmented-wave (PAW) potentials were used.

A plane-wave energy cutoff of $E_{cut} = 500$ eV was used and the Brillouin zone was sampled with a 2x2x1 Monkhorst-Pack k-point mesh. The calculations were performed using HPC resources from CALMIP. For a standard calculation run (e.g. geometry optimization, frequency calculations, etc.), 4 input files were required shown in Table 2.2. After a VASP run, different output files were created, which depended on the task performed. The most important output files in this work and their description are shown in Table 2.3.

Table 2.2 Input files for a standard calculation via VASP.

File name	Function [40]
INCAR	contains the input parameters that control the calculations
POSCAR	holds the details on the structure (dimension of the super cell, amount and positions of the different atoms)
KPOINT	defines the k-point coordinates
POTCAR	contains the relevant information of the pseudo potentials in the order of the positions given in the POSCAR

Table 2.3 Output files for a standard calculation via VASP.

File name	Function [40]
CONTCAR	holds the details on the relaxed structure (dimension of the super cell, amount and positions of the different atoms)
OSZICAR	contains a summary of results
OUTCAR	contains the detailed results of the VASP run

2.6.1 In_2O_3(111) Surface

The supercell for the stoichiometric (111) surface of In_2O_3, which is the thermodynamically most stable one [41], contained a total number of 64 indium and 96

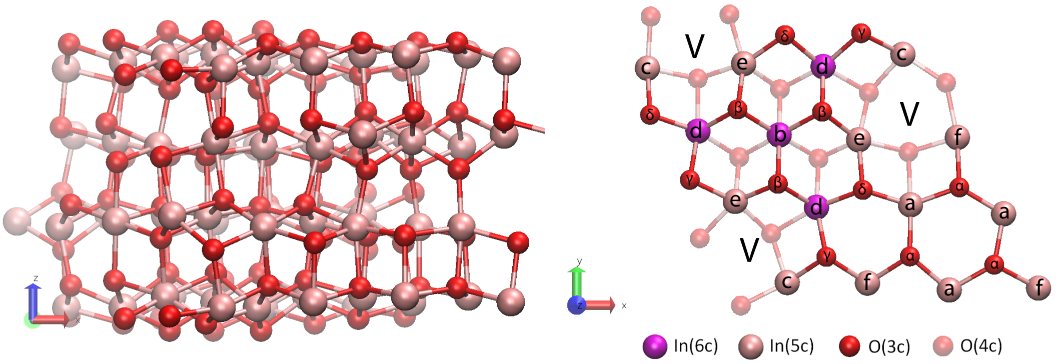

(a) Side view of the $In_2O_3(111)$ super cell containing 64 indium and 96 oxygen atoms. The top half represents the surface while the bottom half simulates the bulk.

(b) Top view of the primitive unit cell. Purple and pink represent 6-fold and 5-fold coordinated In atoms, respectively. O is shown in red.

Figure 2.7 $In_2O_3(111)$ from (a) the side view and (b) the top view.

oxygen atoms. This corresponds to a cell dimension of 14.63x12.68x25.00 Å^3 with a surface area of 162.18 Å^2. The surface structures were represented by periodically repeated slabs separated by a vacuum zone of $\sim$ 15 Å in z direction. In all calculations the atoms in the bottom half were frozen at their equilibrium bulk position to simulate a bulk effect. The atoms in the top half and the adsorbates were allowed to relax. The super cell is depicted in Figure 2.7(a).

The primitive unit cell (1x1) with a stoichiometric surface exhibits 16 In and 24 O atoms with three vacant oxygen sites, labeled V, seen as interstitial site (see Figure 2.7(b)). 4 In atoms are six-fold coordinated In(6c) in two inequivalent positions, labeled b and d, and 12 are five-fold coordinated In(5c) in four inequivalent positions, labeled a, c, e, and f. The atoms are labeled according to [30]. Half of the 24 oxygen atoms are three-fold coordinated called out-of-plane (oop) oxygen atoms since they sit above the In layer and are denoted as O_O. They occupy four symmetrically inequivalent sites labeled α, β, γ and δ. The other half is below the In layer with four-fold coordination labeled in-plane (ip) oxygen. In order to display all images presented in this work the visualization program Visual Molecular Dynamics (VMD) [42] was used.

The relative energies ΔE in this work were calculated with the following equation:

$$\Delta E = E_{adsorbed/dissociated\ molecule\ on\ the\ surface} - (E_{surf} + E_{gaseous\ molecule}) \qquad (2.4)$$

where $E_{adsorbed/dissociated\ molecule\ on\ the\ surface}$ represents the total energy of the system with an adsorbed or dissociated molecule on the surface, E_{surf} and $E_{gaseous\ molecule}$ the relaxed surface and gaseous molecule, respectively. Negative values indicate exothermic adsorption and favorable processes.

2.6.2 Calculation of the Vibrational Wavenumbers

In order to gain information about the experimentally observed wavenumbers in the DRIFTS measurements, a computational investigation on the spectroscopic properties was done. After relaxing the cell, the final CONTCAR was used as POSCAR-input for the VASP run. The calculation of the vibrational frequencies was based on the density-functional perturbation theory (DFPT) [43] which was implemented in VASP using tag `IBRION = 7` in the INCAR file. It created the Hessian matrix (matrix of second derivatives), a secondary file called DYNMAT. This file is needed for phonon calculations. After the VASP run, all values were printed at the end of the OUTCAR file. Out of the OUTCAR file, the frequencies were extracted. By specifying `LEPSILON=.TRUE.` in INCAR, not only the vibrational intensities were calculated but also the born effective charges, piezoelectric constants and the ionic contributions to the dielectric tensor were determined [44]. The energy cutoff E_{cut} was set to 500 eV. The calculated vibrational modes were visualized using Molden [45, 46]. This way, the calculated wavenumbers could be assigned easily to the corresponding modes.

3

Sensing with In_2O_3

3.1 Material Characterization

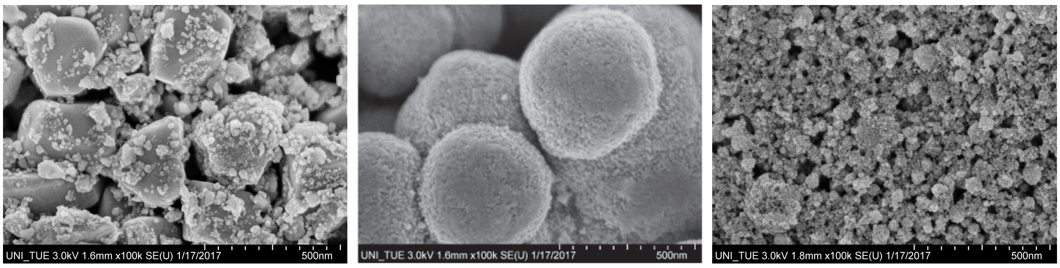

(a) SA **(b)** IC1 **(c)** IC2

Figure 3.1 SEM images of the sensing layers of SA, IC1 and IC2.

The first set of analyses investigated the morphological and structural characteristics of the different In_2O_3 materials. For this purpose, SEM images and XRD patterns of the sensitive layers were acquired. Starting with the SEM images (Figure 3.1) the SA layer shows a large size and shape particle distribution; the particles range from 10 nm to almost two microns. However, it is unclear whether the large particles are monocrystalline or agglomerates of smaller particles. In the case of IC1, the layer consists of large porous spherical agglomerates of smaller particles between 10 and 20 nm. The layer based on IC2 seems to be less agglomerated and the crystallite size was found to be between 15 and 20 nm.

The recorded XRD patterns of the sensitive layers, shown in Figure 3.2, are in good agreement with the reference ICSD 14388. To identify reflexes from the substrate, an unprinted sensor was also measured. The XRD patterns of all sensitive layers show a strong reflex intensity at 30.6 ° corresponding to a preferred orientation along the (222) crystallographic plane. Further characteristic reflexes at 35.4, 51.0 and 60.6 ° are observable for all materials which can be assigned to the cubic

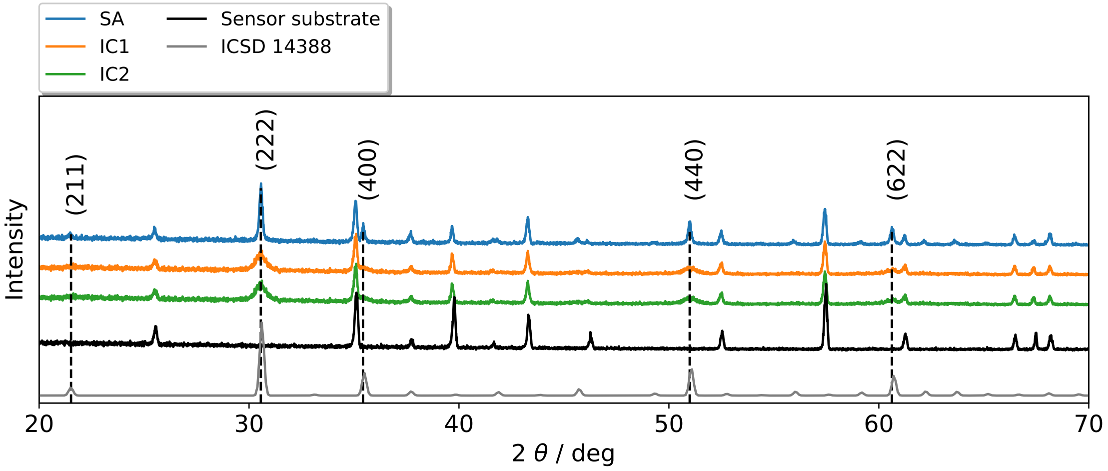

Figure 3.2 XRD diffractogram of the sensing layers of SA, IC1 and IC2 [32].

bixbyite structure of In_2O_3. It is also observable that SA has a higher crystallinity than the home-made materials IC1 and IC2, indicated by the sharp peaks in the pattern. The reflexes of IC1 and IC2 are broadened and indistinct. Using the Scherrer equation, the average crystallite size τ can be estimated [47]:

$$\tau = 2 \cdot \sqrt{\frac{\ln(2)}{\pi}} \cdot \frac{\lambda}{b_{1/2} \cdot \cos(\theta)} \tag{3.1}$$

where λ represents the X-ray wavelength in ångström, $b_{1/2}$ the line broadening at half the maximum intensity in radian and θ the Bragg angle in degree [47]. For the calculation, the most intense peak at 30.6 ° was fitted with the Gaussian function. The average diameters of the crystals were found to be 50 nm for SA, 14 nm for IC1 and 16 nm for IC2. The calculated size and the SEM image of SA do not fit well together. Large particles (over 100 nm) have a large instrumental error due to the small width of the reflexes [47]. This makes the calculated crystallite size for SA unreliable. The calculated sizes of IC1 and IC2 fit well to the SEM images [32].

3.2 DC Resistance Measurements

Water vapor is the most common interfering analyte in atmospheric air. It is known to have a reducing effect on n-type semiconductors [11]. WO_3 is an exception; it shows an oxidizing effect under water vapor exposure [48]. Recently, it has been shown, that depending on the surface orientation of SnO_2, water either has a huge reducing effect or does not change the resistance at all [24]. In order to investigate how In_2O_3 changes its resistance when exposed to H_2O and if the

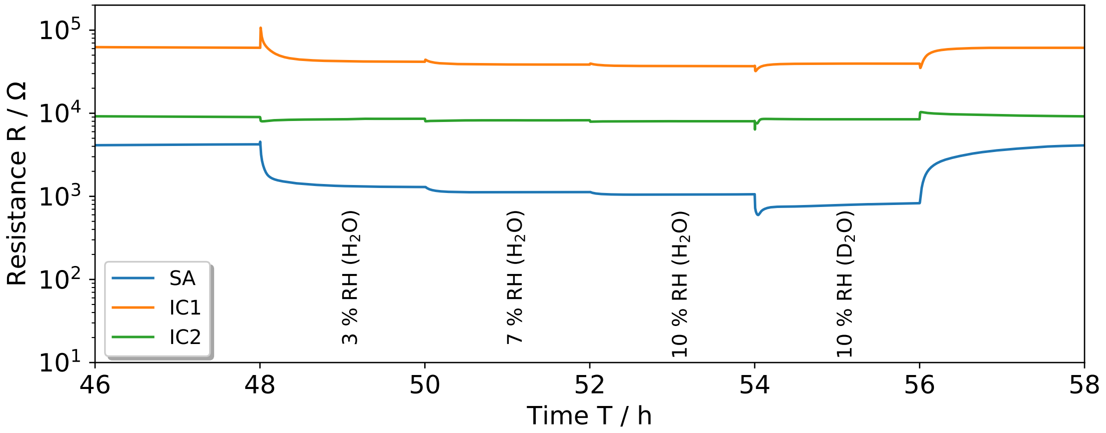

Figure 3.3 DC resistance measurements of the sensors SA, IC1 and IC2 at 300 °C under 3, 7, 10 % H_2O and 10 % D_2O in syn. air.

synthesis route makes a difference, the DC resistance under water vapor exposure (3, 7, 10 % relative humidity (RH) @ 25 °C) in syn. air was recorded, shown in Figure 3.3. It is interesting that the effects of humidity are different for the differently prepared materials: for SA, the resistance change between dry and 3 % RH produces a sensor signal of 3.2. The change from 3 % to 10 % RH is minimal – total sensor signal for 10 % RH is 4. For IC1 the change in resistance is much less significant, the sensor signals range from 1.4 for 3 % RH to 1.6 for 10 % RH, while for IC2 the effect is negligible, as already reported in [33].

The presence of humidity not only changes the baseline resistance but also affects the sensor response to different analyte gases. In this chapter, CO will be considered as an analyte gas. Figure 3.4 shows the effects of CO exposure (25, 45, 100, 300, 500 ppm) in dry and humid conditions (10 % RH @ 25 °C). Also here, the differently prepared materials show different behavior. This is apparent when the sensor signals to 500 ppm CO are examined, shown in Figure 3.5(a). For SA, the presence of humidity decreases the sensor signal from 20 in dry conditions to 10. For IC1 the decrease is from 10 to 9 and for IC2 there is no impact (sensor signal 12 in both conditions). Additional information can be gained from the raw resistance data during the exposure to 500 ppm CO (Figure 3.5(b)). All three In_2O_3 gas sensors show very similar resistance values during CO exposure in dry, as well as in humid conditions. The differences in sensor signal thus are determined by the different impact of humidity on the baseline resistance. These results indicate that humidity and CO have the same adsorption sites and reaction partners on the surface of In_2O_3.

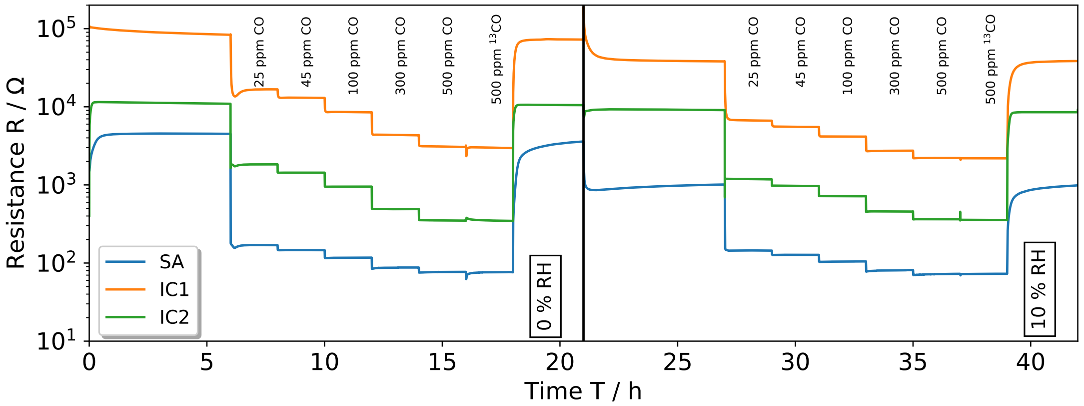

Figure 3.4 DC Resistance measurements of the sensors SA, IC1 and IC2 at 300 °C under 25, 45, 100, 300, 500 ppm CO and 500 ppm ^{13}CO in dry syn. air and 10 % RH [32, 33].

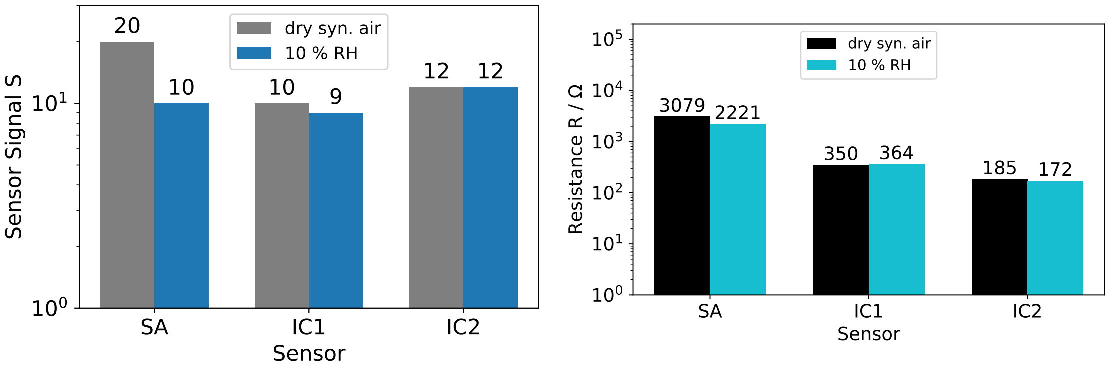

(b) Resistances of SA, IC1 and IC2.

(a) Sensor signals of SA, IC1 and IC2.

Figure 3.5 Sensor signals and resistances of the sensors at 300 °C under 500 ppm CO exposure in dry syn. air and 10 % RH [32, 33].

3.3 Identification of the In-O Bands

The most widely accepted sensing mechanism for SMOX gas sensors involves negatively charged oxygen adsorbates and their reaction with analyte gases. The ionosorption of oxygen causes an electron depletion layer at the surface. The reaction with reducing gases, e.g. CO or H_2, leads to a decrease of this depletion layer changing the resistance of the material [11]. A classical approach to understand the role of adsorbates on the surface of SMOX gas sensors is to use operando DRIFT spectroscopy [49–51]. In order to gain additional insight into the surface chemistry and to support the assumptions based on the DC resistance evaluation, *in-situ*/operando DRIFT spectroscopy was performed.

In a first step, according to the investigation procedure described in [52], the reactivity with humidity, CO and H_2 was investigated. The three sensors were exposed to 500 ppm CO/^{13}CO, 250 ppm H_2/D_2 and 10 % water vapor and heavy water vapor @ 25 °C in a background of dry syn. air. Additionally, the sensors were exposed to 1000 ppm O_2 in a background of N_2.

This series of measurements allows the differentiation between the different surface species, In-O overtones, carbonates and hydroxyl groups, that are responsible for the IR bands in the region between 1700 and 1000 cm^{-1}. For example, one expects that the bands that increase during exposure to O_2 in a background of N_2 and decrease because of exposure to humidity, CO and H_2 indicate the formation or cancellation of In-O bonds. The other bands can in this way be attributed to hydroxyls or carbonates and the use of isotopically labelled water vapor and CO allows discrimination between hydroxyls and carbonates. Before describing the roles of hydroxyl groups and carbonates, the In-O bands were identified. The infrared spectra under CO, H_2, water vapor in syn. air and O_2 in N_2 are shown in Figure 3.6. The corresponding wavenumbers $\widetilde{\nu}$ are listed in Table 3.1.

In Figure 3.6 one can see that under O_2 exposure in N_2, all materials show several increasing bands between 1600 and 1000 cm^{-1}. For the SA sample, bands centered at 1512, 1271, 1117 and 1024 cm^{-1} are visible. They decrease when the sensor is exposed to reducing gases in syn. air and do not shift during H_2O/D_2O experiments (see Figure 3.7), which indicates that they are the In-O bands of this material. The H_2O/D_2O experiments are described in more detail in the following paragraph. In the same manner it was found that bands centered at 1559, 1523, 1262, 1222, 1104 and 1003 cm^{-1} are the In-O bands of IC1 and bands centered at 1536, 1500, 1305, 1266, 1105 and 1030 cm^{-1} are the In-O bands of IC2.

These results show that for all materials CO, H_2 and water vapor react with surface oxygen and exposure to them increases the concentration of surface oxygen vacancies. In the case of H_2O exposure, decreasing In-O bands could also indicate the formation of hydroxyl groups. The observed reduction of all materials under water vapor exposure would determine a decrease of the sensor resistance. The observed differences can be related to the different extents of the reduction and/or to additional surface processes.

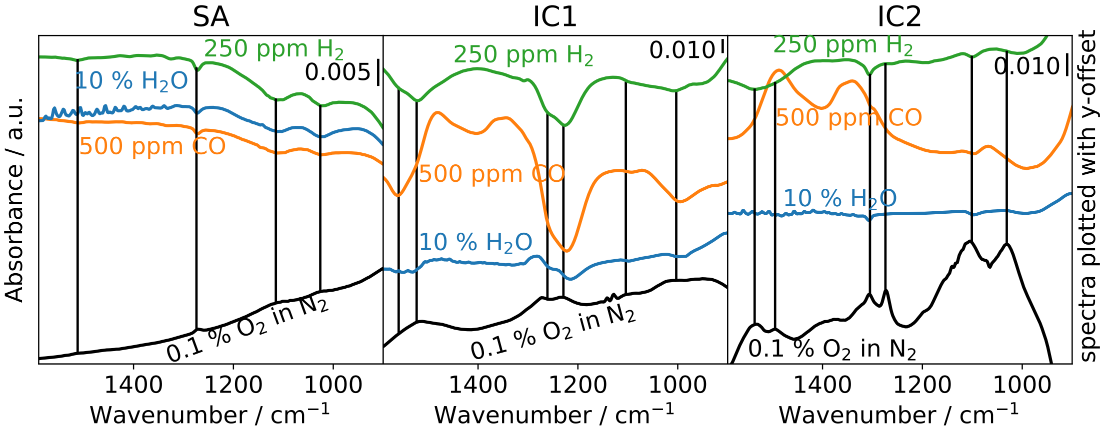

Figure 3.6 Absorbance spectra of SA, IC1 and IC2 under 1000 ppm O_2 exposure in N_2, 250 ppm H_2 exposure, 500 ppm CO exposure and 10 % water vapor in dry syn. air at 300 °C; reference spectra: nitrogen and dry syn. air, respectively.

Table 3.1 Corresponding wavenumbers to the spectra in Figure 3.6.

Material	$\tilde{\nu}$ / cm^{-1}	Material	$\tilde{\nu}$ / cm^{-1}	Material	$\tilde{\nu}$ / cm^{-1}
SA	1512	IC1	1559	IC2	1536
SA	1271	IC1	1523	IC2	1500
SA	1117	IC1	1262	IC2	1305
SA	1024	IC1	1222	IC2	1266
		IC1	1104	IC2	1105
		IC1	1003	IC2	1030

3.4 Reaction of Water Vapor

It is widely accepted that humidity exposure results in hydroxyl groups [11]. Although many efforts have been made to understand and model the reaction between water vapor and SMOX gas sensors [11,50,53], the surface processes are not completely understood. Recently it was shown that the different processes under water exposure have varying electrical effects, depending on the nature of the material and surface orientation [24,48]. In section 3.2, it has been demonstrated that different In_2O_3 materials can have different responses to H_2O as well. In order to understand the differences between the materials and the sensing mechanism, it is very important to identify the hydroxyl groups.

The use of an exchange experiment, water vapor with deuterated water vapor, has been proven very useful in unambiguously identifying hydroxyl groups [50,52]. Due to the exchange of hydrogen with deuterium, a shift in the IR spectra is visible. The sensors were exposed to 10 % H_2O @ 25 °C followed by 10 % heavy water vapor @ 25 °C, and simultaneously infrared measurements were performed. The spectra were referenced to dry syn. air. The obtained spectra are shown in Figure 3.7.

The findings indicate that for all materials the positions of the bands identified as In-O bonds do not change, which further confirms their attribution. Even though all materials show decreasing In-O bands, the decrease for SA is more significant than for IC1 and IC2. Some other differences between the materials are obvious in the spectral region corresponding to the hydroxyl stretching bands (between 3700 and 3100 cm^{-1}) [54]. The bands associated with hydroxyl groups is further proven by their replacement with the corresponding OD groups, which is visible through the shift towards lower wave numbers (between 2750 and 2430 cm^{-1}) that takes place in the H_2O/D_2O exchange experiments. The wavenumbers corresponding to the center of the O-H and O-D bands as well as the calculated shift factors can be found in Table 3.2.

The calculated shift factors are between 0.737 and 0.740 which are in good agreement with the theoretical shift factor of 0.728. This value was calculated based on the harmonic oscillator approximation:

$$\frac{\widetilde{\nu}_{\mathrm{D_2}}}{\widetilde{\nu}_{\mathrm{H_2}}} = \sqrt{\frac{\mu_{\mathrm{D_2}}}{\mu_{\mathrm{H_2}}}} \tag{3.2}$$

The reason for the slight difference between the observed and theoretical shift factor is, that for the calculation the harmonic oscillator approximation was considered. For a better calculation, the anharmonic oscillator has to be chosen.

The band centered at 3230 cm^{-1} that is present in the SA spectra does not belong to hydroxyl groups. This is demonstrated by the fact that it does not change position under exposure to D_2O. It is an artefact of ice on the detector, which loses vacuum. When the detector is evacuated, that broad band disappears.

In the literature, three categories of M-OH groups are described: isolated terminal, interacting terminal and rooted. Bands above 3700 cm^{-1} are considered to be stretching vibrations of isolated terminal hydroxyl groups. Those of the interacting terminal and rooted groups occur below 3700 cm^{-1} because the additional coordination reduces the vibration frequency [55]. For SnO_2, depending on the

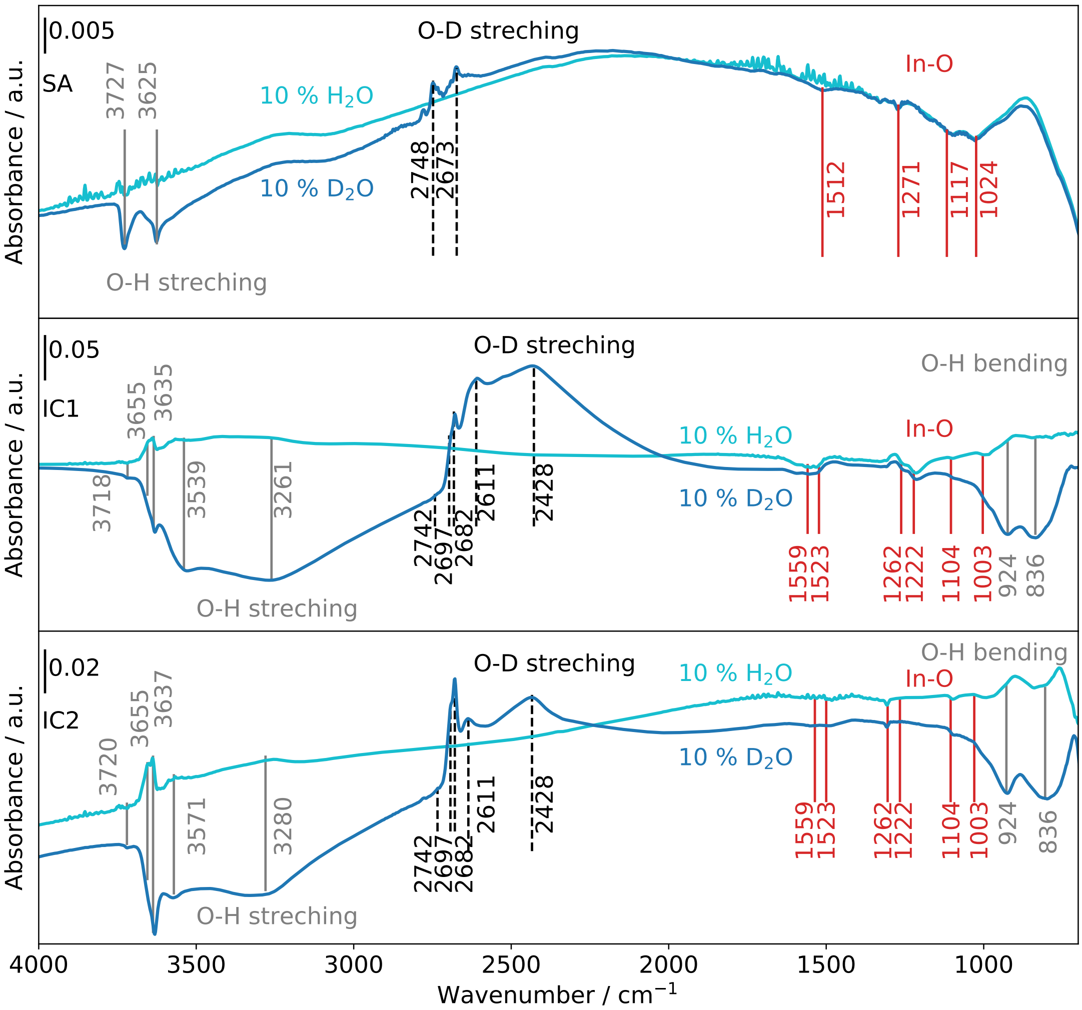

Figure 3.7 Absorbance spectra of SA, IC1 and IC2 under 10 % water and 10 % heavy water vapor at 300 °C operation temperature; reference spectra: dry syn. air [33].

orientation of the surface, the formation of terminal and rooted hydroxyl groups has different electrical effects [24]. At this point, based on DRIFT spectra, it is difficult to tell whether the hydroxyl groups present on the surface of the In_2O_3 materials are terminal or rooted. For In_2O_3 the different facets in combination with water vapor have not yet been investigated in detail. Thus, it is problematic to make any distinct statements about the nature of the hydroxyl groups of these materials. However, the DFT calculations of Wagner at al. gave a first hint that under H_2O exposure on the surface of $In_2O_3(111)$ only rooted OH groups would form [30]. The DFT calculations of the second stable surface $In_2O_3(110)$ [56] with dissociated H_2O, contrarily, indicated a combination of terminal and rooted groups [57]. It is still, however, unclear which IR band would be indicative of either and what electrical effect they would have. Since all three materials show the

Table 3.2 Corresponding wavenumbers of the hydroxyls to the spectra in Figure 3.7 and the shift factors.

Material	$\widetilde{\nu}$ (O-H) [cm^{-1}]	$\widetilde{\nu}$ (O-D) [cm^{-1}]	Shift factor
SA	3727	2748	0.737
SA	3625	2673	0.737
IC1	3718	2742	0.737
IC1	3655	2697	0.738
IC1	3635	2682	0.738
IC1	3539	2611	0.738
IC1	3261	2428	0.745
IC2	3720	2742	0.737
IC2	3655	2697	0.738
IC2	3637	2682	0.737
IC2	3571	2611	0.731
IC2	3280	2428	0.740

same preferred orientation in the XRD patterns (see Section 3.1), it is assumed that they have the same dominant face (111). Therefore it is concluded that, presumably, on the surface of SA, IC1 and IC2 mainly rooted hydroxyl groups are present.

A different explanation is needed for the variation in the electrical effect of water vapor. If one considers the presence of different bands not as variations in coordinated hydroxyl groups but as indicators for different initial levels of hydroxylation, a correlation to the different behavior of the three materials during humidity exposure can be seen. While SA only has a low amount of hydroxyl groups on the surface, as indicated by the two exchanging bands centered at 3727 and 3625 cm^{-1} in Figure 3.7, IC1 and IC2 have large amounts of hydroxyl groups, which are located between 3718 and 3261 cm^{-1} for IC1 and between 3720 and 3280 cm^{-1} for IC2. These two materials additionally show bands centered at 924 and 836 cm^{-1} for IC1 and 928 and 805 cm^{-1} for IC2 which can be assigned to the O-H bending modes [58, 59]. This assumption means that for SA an increase of the humidity leads to a hydroxylation of its surface (since it has less hydroxyls initially) and consequently to a greater change in the resistance, whereas IC1 and IC2 already have a high amount of hydroxyl groups on the surface and as a result less adsorption and dissociation sites for additional hydroxyls. The change in the resistance is thus lower. This also goes along with the intensity of the decreasing In-O bands between the materials. It is possible that the saturation of the two homemade materials with hydroxyl groups on the surface already happens in dry syn. air since the bottle contains around 11 ppm H_2O (see Appendix, Figure 5.1).

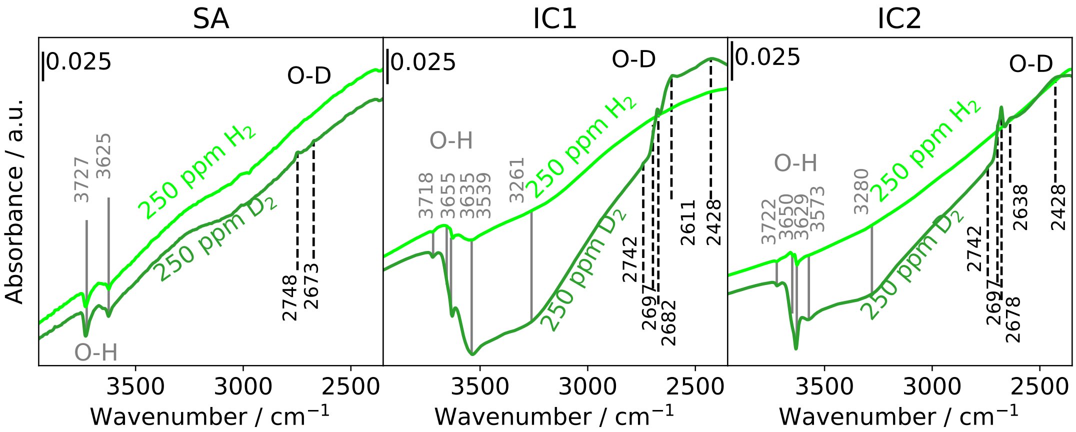

Figure 3.8 Absorbance spectra of SA, IC1 and IC2 under 250 ppm D_2 and 250 ppm H_2 exposure in dry syn. air at 300 °C operation temperature; reference spectra: dry syn. air.

To prove this assumption, D_2/H_2 exchange experiments were performed in dry syn. air. Exposure to D_2 at the beginning causes an exchange of the hydrogens of the hydroxyl groups on the surface which are already formed in dry syn. air by deuterium. The results, shown in Figure 3.8, demonstrate that the exchanging groups are the same as under humidity exposure, confirming the conjecture that they already exist in dry conditions.

3.5 Reaction of CO in Dry Air and Humidity

In section 3.2, it was shown that humidity affects the response of the materials to CO differently. In order to investigate and understand the differences, again, DRIFT spectra were recorded while the materials were exposed to 500 ppm CO/^{13}CO in dry syn. air and in 10 % RH. The spectra are shown in Figure 3.9.

Similar to humidity exposure, CO exposure results in a decrease of the In-O bands for all the materials. This indicates a surface reduction process. An additional proof for the reduction of the surface is the formation of gas phase CO_2 as indicated by the asymmetric stretching mode centered at 2349 cm^{-1}. Since CO_2 is in the gas phase, the molecule can rotate, and thus the rotational structure is visible. The resolution of the spectra is not high enough to observe the separation between the rotational lines, which is the reason why only two broad bands are observable. However, the splitting would not be observable if CO_2 was adsorbed on the surface [60].

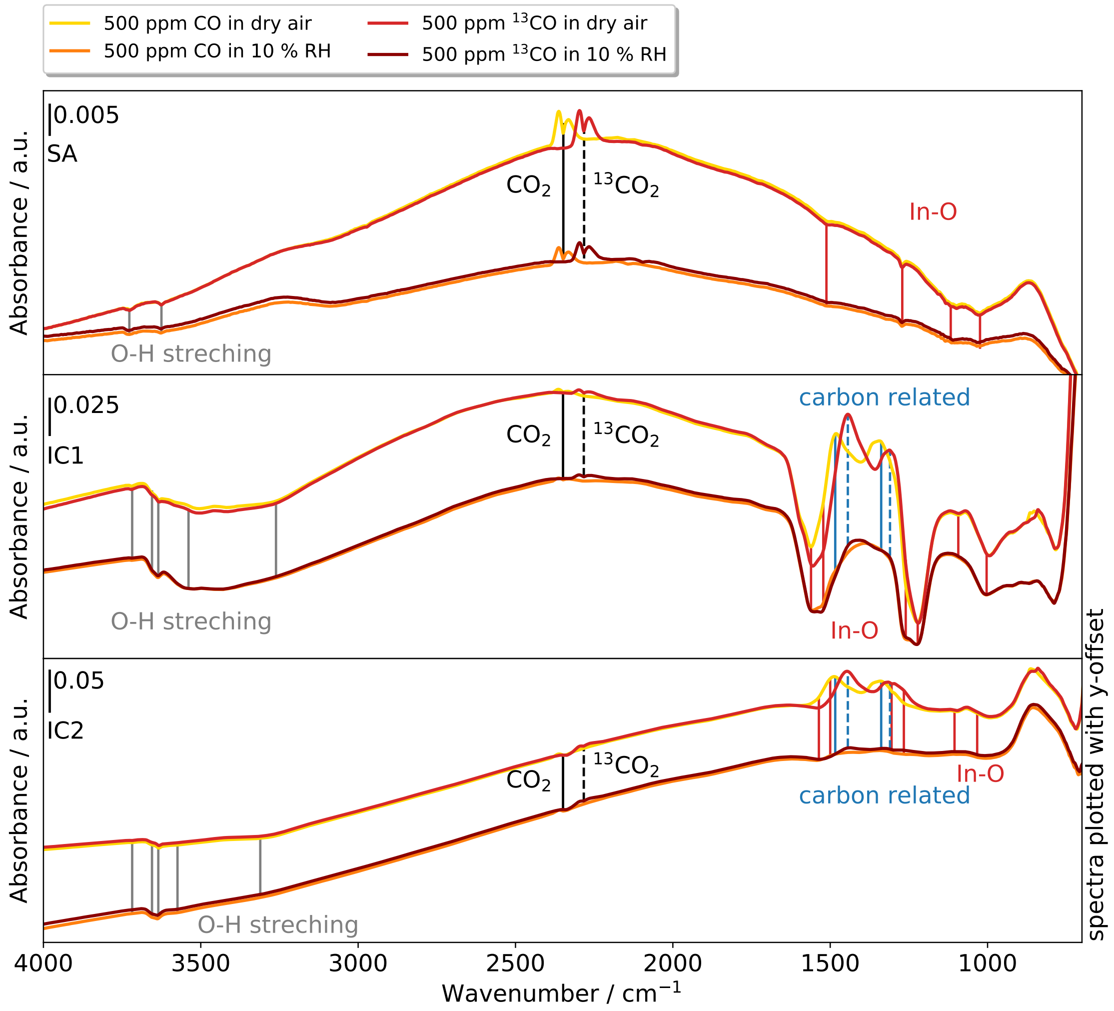

Figure 3.9 Absorbance spectra of SA, IC1 and IC2 under 500 ppm CO and 500 ppm ^{13}CO exposure in dry and humid air; reference spectra: dry syn. air and 10 % RH [33].

In the O-H stretching region, the decrease of the hydroxyl concentration can be observed for all materials. This indicates a dynamic process which can be expressed by two reaction equations [50]:

$$H_2O_{gas} + O^{\alpha-} \rightleftharpoons 2\,OH + \alpha e^- \tag{3.3}$$

$$O^{\alpha-} + CO \longrightarrow CO_2 + \alpha e^- \tag{3.4}$$

Since it has been shown that even in dry air around 11 ppm H_2O is present, it can be assumed that there is an equilibrium between water vapor, surface oxygen and hydroxyls as shown in Eq. 3.3. Through the reaction of CO with surface oxygen (Eq. 3.4), the concentration of O on the surface decreases which leads to a shift of the equilibrium in Eq. 3.3 to the left showing a decrease of the hydroxyl concentration [50]. This also suggests that the total number of the surface adsorption sites for both H_2O and CO is limited. They have the same reaction partner on the surface which explains why the absolute resistance under CO exposure is constant but the signal changes in the presence of humidity.

In the case of IC1 and IC2, additional increasing bands are visible during CO exposure. Based on an isotopic exchange experiment between 500 ppm CO and ^{13}CO, the carbon related and non-carbon related surface species can be identified. Here, a shift to lower wavenumbers with a factor of about 0.973 will be caused by the replacement of ^{12}C by ^{13}C. The samples show bands centered at 1480 and 1348 cm^{-1}. In the exchange experiment these bands are shifted to 1442 and 1311 cm^{-1} and the corresponding shift factors are for both 0.97. Bands in this region can be attributed to surface carbonates or bicarbonates. Their formation, albeit significantly reduced, is also observed in the case of 500 ppm CO exposure in the presence of humidity (10 % RH @ 25 °C). The formation of carbon related species is not observable for SA.

A similar observation has been reported for SnO_2. Degler et al. investigated two different tin dioxide materials. They show that the reaction with CO results in carbonates on one SnO_2 material but not on the other. To understand if carbonates were intermediates of the reaction with CO and surface oxygen or if they form through a secondary reaction with CO_2, both sensors were exposed to carbon dioxide in dry air. They found that the same carbonates form as during CO exposure and concluded that their formation is caused by a subsequent reaction with CO_2 with SnO_2 [52].

Here the same procedure was applied. All sensors were exposed to 500 ppm CO_2 in dry syn. air and additionally in 10 % RH to investigate the role of humidity. The DRIFTS results are shown in Figure 3.10. SA shows no carbon related surface species, while IC1 and IC2 show the same bands as during CO exposure. It is evident that also for In_2O_3, their formation is a result of a subsequent reaction with CO_2. It is also observable, that there are increasing and at the same time decreasing hydroxyl bands above 3500 cm^{-1}, which indicates their participation in the formation of these surface species. This already indicates that not carbonates but bicarbonates are formed on the surface. Their formation shows no significant change in the resistance (see Appendix, Figure 5.2) and is significantly hindered

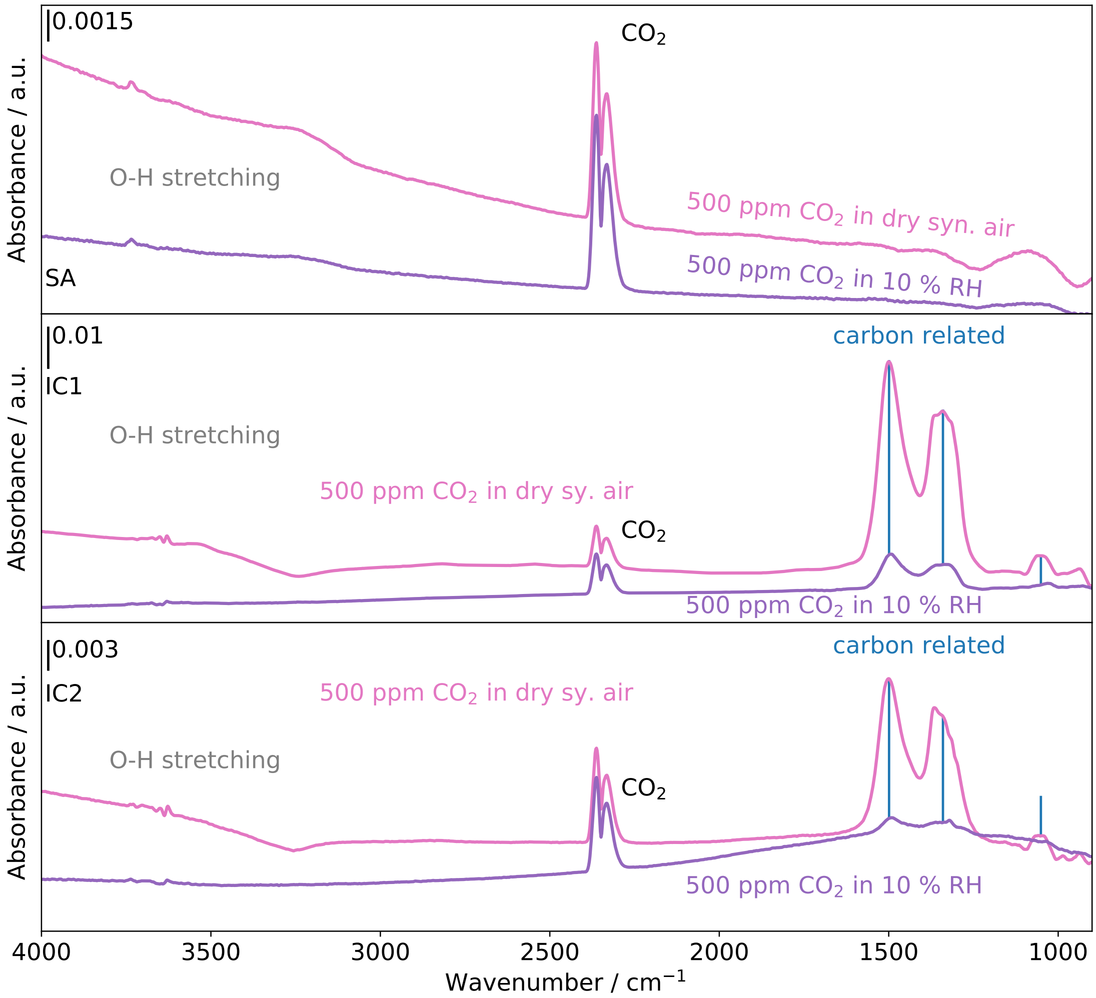

Figure 3.10 Absorbance spectra of SA, IC1 and IC2 during 500 ppm CO_2 exposure in dry air and 10 % RH; reference spectra: dry syn. air and 10 % RH, respectively.

in humid conditions. The findings suggest that H_2O and CO_2 have the same adsorption sites on the surface of In_2O_3.

A close look at this species and the surface hydroxyls in Figure 3.9 reveals an interesting relation and provides a possible explanation: it seems like that there is a correlation between the amount of hydroxyl groups and the formation of carbon related surface species. IC1 and IC2 initially have a large amount of hydroxyl groups on the surface and show carbon related species, SA only shows low initial hydroxylation and no carbon related groups. It appears that highly hydroxylated surfaces favor the formation of these species on the surface. Similar results have been reported by Baltrusaitis et al. on Fe_2O_3 and Al_2O_3 where they observed the formation of different carbon related surface species involving hydroxyl groups [61].

3.6 Measurements in N_2

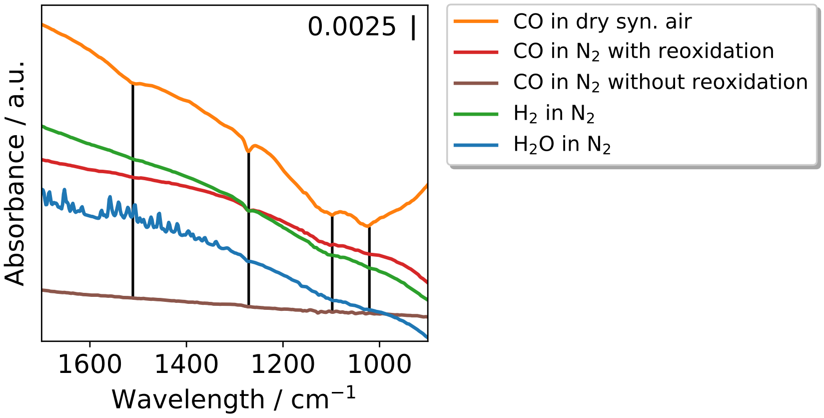

Figure 3.11 Absorbance spectra of SA under 500 ppm CO in dry syn. air, in 500 ppm CO, 250 ppm H_2 and 10 % RH in N_2; reference spectra: dry syn. air and N_2, respectively.

The measurements in the previous sections were done in syn. air where the reoxidation of the material through atmospheric oxygen can readily take place. For SnO_2 and WO_3, at least during CO exposure, it is known that the surface lattice oxygen is the reactive species [52, 62]. From the measurements in this work, it is not clear, if the surface lattice oxygen or some other sort of adsorbed molecular or atomic oxygen ion is the reactive surface partner.

Since SA shows no carbonates and hydroxylate related species in the In-O overtone region, which could disturb the assignment of the changing bands, the measurements with this material were repeated under 500 ppm CO, 250 ppm H_2 and 10 % RH using N_2 as a carrier gas. If adsorbed molecular/atomic oxygen is the main reaction partner, it is assumed that in its absence, no surface reactions will take place because no reaction partners for the analyte gases are present. On the other hand, if the surface lattice oxygen is the reaction partner, one would expect a decrease of the In-O bands even in the absence of atmospheric oxygen.

For this purpose, first the sensor was kept in syn. air and afterwards in N_2 until a stable baseline was reached. The sample was then exposed to the various analyte gases. The absorbance spectra are shown in Figure 3.11.

The bands identified as In-O during syn. air measurements, are found to decrease in the presence of all three reducing gases. The second measurement under CO exposure was done without letting the sensor getting reoxidized. This measurement shows no changes of the In-O bands. These findings indicate that lattice metal oxygen is the reactive species as in the case of SnO_2 and WO_3 and further that the reaction only takes place on the surface, since the last measurement of CO without letting the material reoxidize shows no changing bands. Consequently, the material is not fully reduced to metallic indium.

3.7 DFT Calculations of H_2O on $In_2O_3(111)$

In order to confirm the assumptions from the last section and to further understand the experimental results, DFT calculations were performed. For the calculations only the (111) surface was considered since it is the most stable one [41, 56]. A stoichiometric structure of indium oxide ($In_{64}O_{96}$) and a reduced surface with an oxygen vacancy V_O ($In_{64}O_{95}$) to simulate a defective surface were used. Each reduced surface was created by removing one out-of-plane (oop) oxygen. Also hydroxylated surfaces were examined.

The DC resistance measurements have shown, that different In_2O_3 materials have different responses to H_2O. The corresponding DRIFTS measurements indicated that they differ in the nature of the hydroxyl groups. Instead of studying different orientations of In_2O_3, which was the case for the DFT calculations of SnO_2 with water [24], a new approach shall be considered in this work: not the surface orientation but the level of hydroxylation will be examined. Also, their position in the unit cell will be considered since the oop oxygen atoms of $In_2O_3(111)$ differ depending on the neighboring indium atoms they have [30].

3.7.1 Adsorption and Dissociation on the Stoichiometric Surface

The DFT calculations in this section on the stoichiometric $In_2O_3(111)$ surface with H_2O are based on the previous investigations from Wagner et al. [30].

Initially, the $In_2O_3(111)$ surface and a gaseous H_2O molecule without interaction are considered, shown in Figure 3.12(a). The reaction begins with the adsorption of H_2O on an oop β-oxygen with one of its hydrogens, see Figure 3.12(b). The corresponding adsorption energy is -0.8 eV. It is expected that H adsorbs on β-oxygen, since this oxygen is the most reactive oop oxygen on the surface [30].

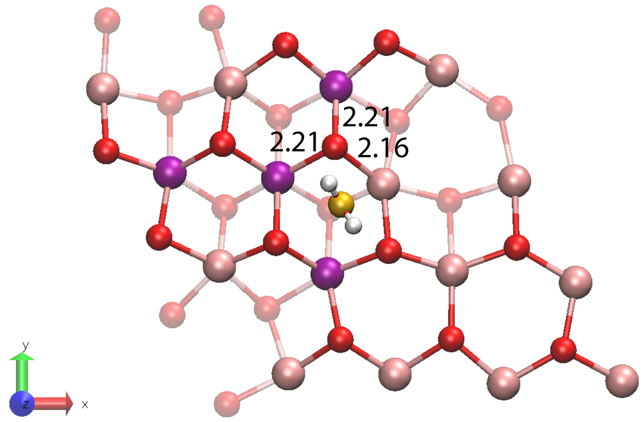

(a) Initial state.

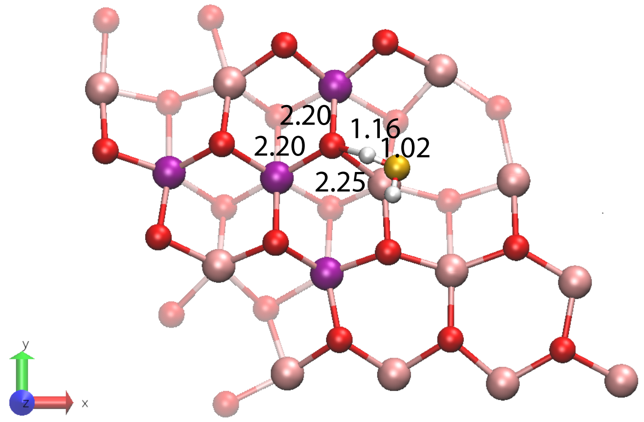

(b) Adsorbed state.

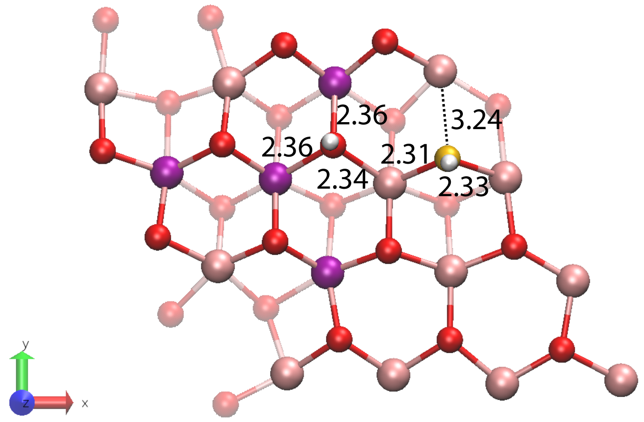

(c) Dissociated state.

Figure 3.12 Adsorption and dissociation of one H_2O molecule on the clean $In_2O_3(111)$ surface. Pink: In(5c), purple: In(6c), red: oop O, light red: ip O, yellow: oxygen from H_2O, white: H.

Overall the length of the In-O bonds change slightly from 2.21, 2.21 and 2.16 Å before interaction to 2.20, 2.20 and 2.25 Å, respectively. Due to the adsorption, a hydrogen bond between β-oxygen and hydrogen of water is created with a length of 1.16 Å. The bond between the adsorbed hydrogen and the oxygen of the water molecule enlarges from 0.98 Å to 1.02 Å. The water molecule thus positions itself into a nearby vacant oxygen site. These surface species already indicate that the adsorbed water molecule might easily dissociate with a certain activation barrier to two hydroxyl groups as was already shown in [30]. In the next step, the adsorbed hydrogen was pushed further to the oop β-oxygen and the water molecule dissociated to two hydroxyl groups; one on the β-O site, denoting it as $O_\beta H$, and the other one occupying one of the vacant oxygen sites between e-In and f-In, labeled $O_V H$, with a two-fold coordination. Both hydroxyl groups are rooted and not terminal. The dissociated situation is shown in Figure 3.12(c). The length of the In-O bonds enlarges to 2.31-2.36 Å. The dissociation is accompanied with an energy gain of -1.4 eV showing that a dissociated water molecule is overall more favorable than an adsorbed one by an energy difference of 0.6 eV, both referenced to a free H_2O molecule without interaction.

For the calculation of the activation barrier, the nudged elastic band (NEB) method was used. This allows the reaction pathways and saddle points to be found when the initial and final states of a reaction are known [63, 64]. In the INCAR-file following parameters were set: `IMAGES = 8` which is the number of images between the initial and final state, `LCLIMB = .True.` which turns on the climbing image algorithm, `ICHAIN = 0` determines the method which should be used (0 for NEB) and `ISPRING = -5.0` which is the spring constant between the images. The energy diagram is shown in Figure 3.13. The activation barrier was calculated to be 0.5 eV.

In order to get an idea, how the two formed hydroxyl groups would appear in an IR-spectrum, the wavenumbers of the dissociated state were calculated (Figure 3.14). The wavenumbers were calculated to be 3717 cm^{-1} for the hydroxyl group $O_\beta H$ formed on the β-site and 3739 cm^{-1} for the hydroxyl group $O_V H$ in the vacant oxygen site. Both are rooted hydroxyl groups which are very close to each other. They show similar wavenumbers which are above 3700 cm^{-1}. This disproves the assumption from the literature that wavenumbers above 3700 cm^{-1} are associated with terminal hydroxyls and the lower ones are attributed to rooted and interacting ones [55].

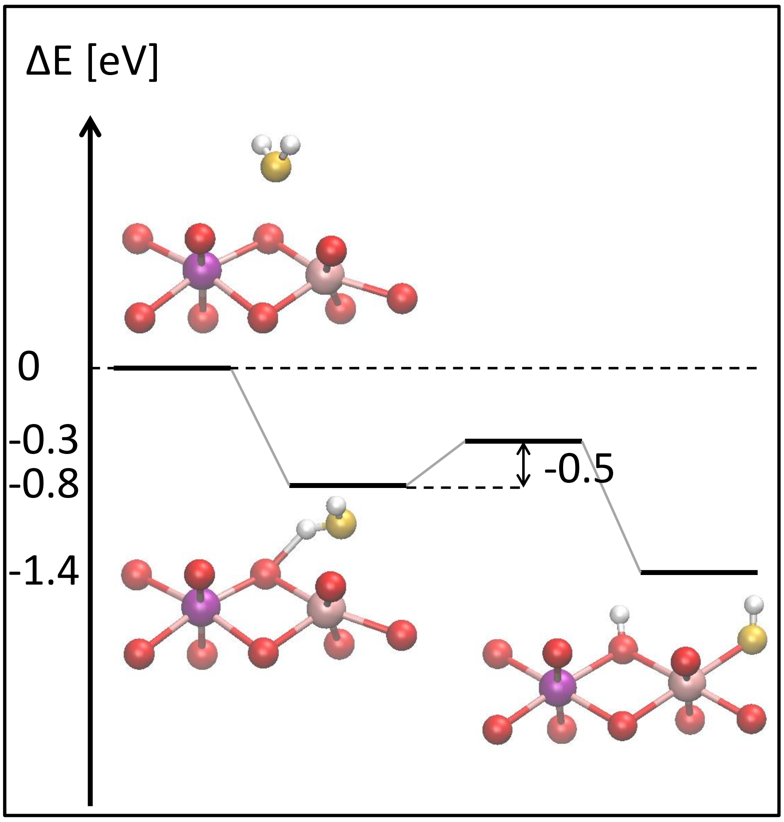

Figure 3.13 Energetic pathway of the adsorption and dissociation of H_2O on the clean $In_2O_3(111)$ surface. The zero reference energy is taken as the water molecule and surface without interaction.

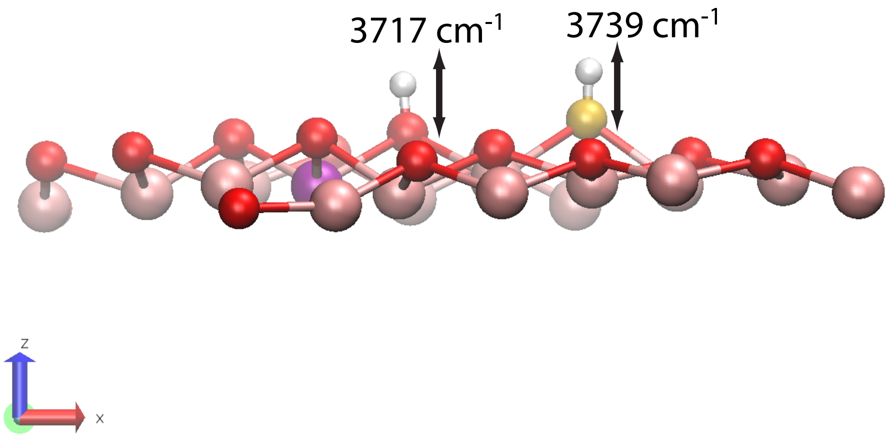

Figure 3.14 Wavenumbers of the two hydroxyl groups formed from the dissociation of one H_2O molecule on the $In_2O_3(111)$ surface.

The calculations show, that the processes of adsorption and dissociation of one water molecule on the perfect surface of $In_2O_3(111)$ is thermodynamically favored and possible with a vacant oxygen site and an unoccupied oop oxygen. During this process, no vacancies are formed. The reaction can be written as

$$H_2O_{gas} + In_{In}{-}O_O{-}In_{In} + In_{In}{-}V_O{-}In_{In} \rightleftharpoons In_{In}{-}O_OH{-}In_{In} + In_{In}{-}OH{-}In_{In} \tag{3.5}$$

which shows the formation of two similar hydroxyl groups and an electroneutral process taking place on the surface of In_2O_3.

Wagner et al. have shown, that not only one but three H_2O molecules can adsorb and dissociate to get a fully hydroxylated surface. This is possible due to the three equivalent oop β-oxygen and three vacant oxygen sites on the clean $In_2O_3(111)$ surface which are necessary for a successful reaction of H_2O. The visualization of the calculation of three dissociated H_2O is shown in Figure 3.15.

The dissociation is accompanied by an energy gain of −1.24 eV per dissociated H_2O molecule. The calculated energies of one and three dissociated H_2O are in line with the reported energies of −1.28 eV for one and −1.18 eV [30] for three dissociated water molecules. Although the reaction is the same on all three dissociation sites, there seems to be a difference in the bond lengths between β-oxygen and d-In depending on the amount of dissociated H_2O molecules: while the bond length between β-O and d-In for one dissociated H_2O is 2.36 Å (see Figure 3.12), this increases to between 2.48 and 2.50 Å for three dissociated water molecules, indicated by the dashed lines in Figure 3.15. The reaction in this case can be written as

$$H_2O_{gas} + In_{In}{-}O_O{-}In_{In} + In_{In}{-}V_O{-}In_{In} \rightleftharpoons In_{In}{-}O_OH{\cdots}In_{In} + In_{In}{-}OH{-}In_{In} \tag{3.6}$$

In this case, the first step for the formation of vacancies is indicated, which suggest that the more water molecules dissociate the higher the change in the resistance.

The calculated wavenumbers are between 3754 and 3749 cm^{-1} for the stretching vibration of the O_VH, between 3729 and 3725 cm^{-1} for the stretching vibration of the $O_\beta H$ and 935, 923 and 829 for the bending mode of the hydroxyl groups of O_VH. The adsorption and dissociation energies and the wavenumbers are summarized in Table 3.3.

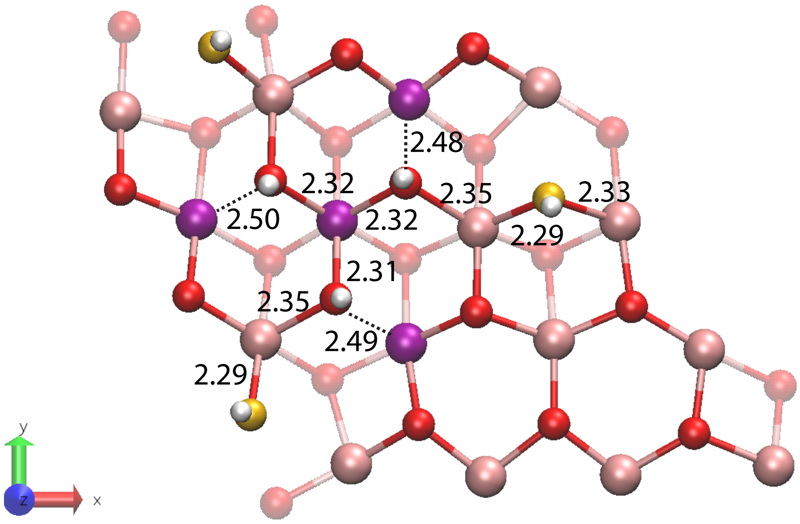

Figure 3.15 Three water molecules dissociated in the unit cell of the In$_2$O(111) surface.

Table 3.3 Energies per molecule and the corresponding wavenumbers of the dissociated water molecules.

Number H_2O	ΔE for one H_2O [eV]	Surface species	Mode	$\tilde{\nu}$ [cm^{-1}]
1	-1.41	O_VH	stretching	3739
		$O_\beta H$	stretching	3717
3	-1.28	O_VH	stretching	3754, 3753, 3749
		$O_\beta H$	stretching	3729, 3727, 3725
		O_VH	bending	935, 923, 829

The results of the calculations show that a In$_2$O$_3$(111) surface does not show any differences between the wavenumbers of the stretching mode regarding one or three dissociated H_2O. The wavenumbers fit very well with the highest wavenumber of 3727, 3718 and 3720 cm^{-1} for SA, IC1 and IC2, respectively. Additionally, the calculations indicate the formation of oxygen vacancies with increasing number of water molecules, which can dissociate on the surface. The ability of this clean In$_2$O$_3$(111) surface to react with water and the enlarging In-O bond length with increasing number of dissociated H_2O molecules confirms the assumption that there are probably fewer hydroxyl groups on the surface of SA with sufficient adsorption and dissociation sites for water vapor to react and change the resistance.

Since only one of the experimentally observed wavenumbers of each material has been found and the others are still missing, different conditions will be considered in the following. In the next step, defects were created by removing various oxygen atoms from the surface to simulate defective conditions which are more likely for metal oxides.

3.7.2 Adsorption and Dissociation on Defective Surfaces

The starting point for the calculations here is a surface with one oxygen less than in the case of the perfect $In_2O_3(111)$ surface. Due to symmetry and periodicity, there are four oop oxygen atoms, which differ from one another (see Section 2.6.1). In order to simulate a defective situation, one oxygen was removed and relaxed which resulted in four different defective surfaces.

The oxygen vacancy creation is highly endothermic with 2.83, 2.90, 3.00 and 3.05 eV for removing β-, δ-, γ- and α-oxygen, respectively. The calculated energies indicate that removing β-oxygen is the most favored while that at α-site is the least favored to generate.

After removing a β-oxygen and putting a water molecule above the vacancy V_β, shown in Figure 3.16(a), the relaxation revealed that the adsorption of water is preferred with its hydrogen on a neighboring β-oxygen and not on a neighboring δ-site, forming a hydrogen bond with a length of 1.62 Å, see Figure 3.16(b). The bond between the hydrogen and oxygen of the water molecule enlarges to 1.04 Å. The bonds between In(6c) and β-oxygen enlarge slightly from 2.16, 2.18 and 2.21 Å to 2.17, 2.24 and 2.23 Å, respectively. By pushing the adsorbed hydrogen towards β-oxygen, the molecule dissociates into two hydroxyl groups; one on the β-site ($O_\beta H$) and the other one healing the vacancy ($O_{V,\beta}H$), see Figure 3.16(c). The bonds between the $O_{V,\beta}H$ and the In atoms are 2.32 and 2.30 Å. The bonds between In(6c) and $O_\beta H$ enlarge further to 2.33 and 2.43 Å, indicating the formation of a vacancy (dashed line). The reaction equation here is the same as in Eq. 3.6, suggesting a decrease in the resistance. The adsorption and dissociation of H_2O is accompanied by an energy gain of -0.95 and -2.23 eV, respectively, which is higher than in the case of the perfect surface (-0.8 and -1.4 eV).

Calculation of the wavenumbers reveal for the $O_\beta H$ group (3719 cm^{-1}) and for the $O_{V,\beta}H$ group (3716 cm^{-1}) that they are largely equivalent and do not differ significantly from $O_\beta H$ groups calculated for the perfect $In_2O_3(111)$ surface (see Table 3.3). The same calculations were done for the oxygen vacancies at the positions γ-, δ- and α-oxygen. For γ- and δ-vacancies, H_2O prefers to adsorb on β-oxygen, and then dissociates to heal the vacancy. The formation of the hydroxyl

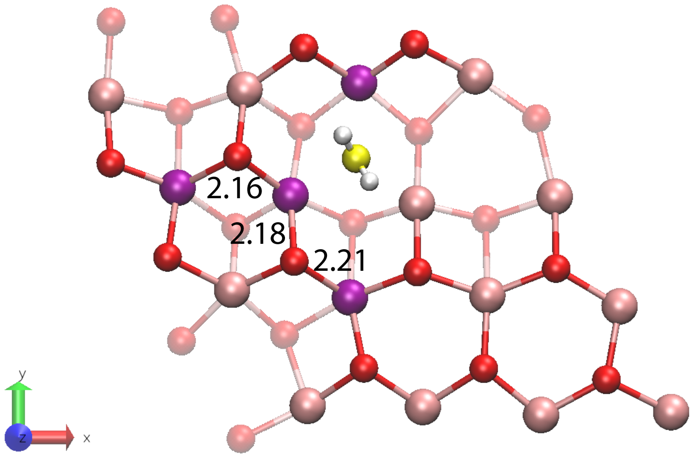

(a) Initial state.

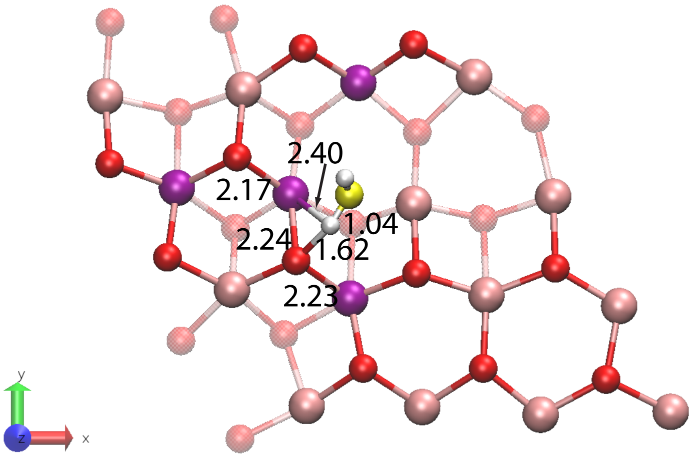

(b) Adsorbed state.

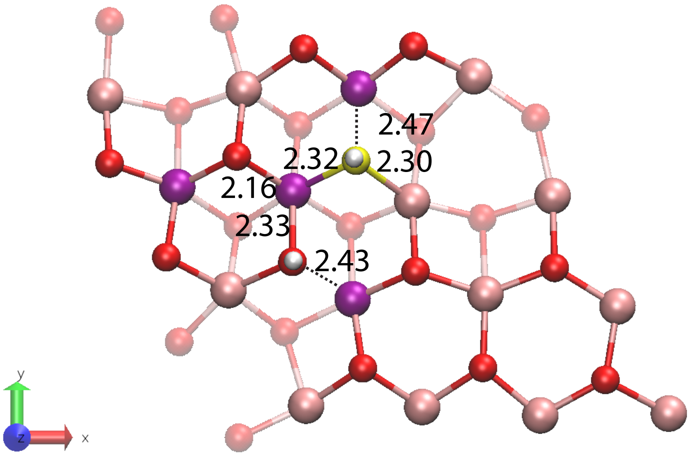

(c) Dissociated state.

Figure 3.16 Adsorption and dissociation of one H_2O molecule on defective $In_2O_3(111)$. Pink: In(5c), purple: In(6c), red: oop O, light red: ip O, yellow: oxygen from H_2O, white: H.

Table 3.4 Calculated energies and wavenumbers of the dissociated water molecules on defective $In_2O_3(111)$.

Vacancy Position	State	ΔE [eV]	Surface species	Mode	$\tilde{\nu}$ [cm^{-1}]
β	adsorbed	-0.95			
	dissociated	-2.23	$O_\beta H$	stretching	3719
			$O_{V,\beta}H$	stretching	3716
δ	adsorbed	-0.68			
	dissociated	-2.16	$O_\beta H$	stretching	3717
			$O_{V,\delta}H$	stretching	3651
γ	adsorbed	-0.82			
	dissociated	-2.21	$O_\beta H$	stretching	3713
			$O_{V,\gamma}H$	stretching	3669
α	adsorbed	-0.62			
	dissociated	-1.83	$O_\gamma H$	stretching	3644
			$O_{V,\alpha}H$	stretching	3632

groups with a vacancy at the position of α-oxygen happens on γ-oxygen. The energy gain of healing the vacancy at the positions γ-, δ- and α-sites are -2.21, -2.16 and -1.83 eV, respectively. The energies and the corresponding wavenumbers are summarized in Table 3.4.

Based on the calculations, the wavenumbers of the hydroxyl groups change depending on the oxygen site, showing a decreasing from β to α. It should be noticed that all are rooted hydroxyl groups, and that not the coordination of the groups but their position in the unit cell result in varying wavenumbers. Additionally, there seems to be a difference in wavenumbers of the hydroxyl group, depending on its neighboring O-H group (compare the wavenumbers 3669 and 3644 cm^{-1} which originate from the same hydroxyl group $O_{V,\gamma}H$ and $O_\gamma H$ but with different neighboring hydroxyls).

Comparison of these results with the results gained from the DC resistance and DRIFTS measurements suggests, that in the case of SA, in addition to the dissociation on a β-O and a vacant oxygen site (see Section 3.7.1) water also dissociates on defects from oxygen vacancies and a neighboring oop oxygen. From the measurements it is known that SA shows a large resistance change and wavenumbers at 3727 and 3625 cm^{-1} during humidity exposure. These findings fit well with the wavenumbers calculated here and the suggested chemical equations in which a vacancy is formed. Also the observed wavenumbers at 3718, 3655 and 3635 for IC1 and 3720, 3655 and 3637 cm^{-1} for IC2 fit to the ones calculated here and in the subsection before but it is more likely that these hydroxyl groups are already formed ones even in very dry air as assumed and discussed in the DRIFTS measurement in Section 3.4. There are still, however, missing wavenumbers from the DRIFTS measurements for IC1 and IC2, which cannot be explained with the results gained so far. More insight will be gained in the following section which considers already highly hydroxylated surfaces.

3.7.3 Adsorption and Dissociation on Hydroxylated and Defective Surfaces

In real conditions, a defective surface can also be highly hydroxylated, modeled by the surface after the dissociation of three water molecules on the β-oxygen and oxygen vacant sites, as shown in Figure 3.15, and removing a γ-, δ- or α-oxygen to simulate a defect. Creating defects at the mentioned positions enables the formation of two further hydroxyl groups with two different dissociation possibilities. As an example, in Figure 3.17, a defect at the δ-position is shown with the two possible dissociation sites (γ- or α-oxygen).

H_2O can adsorb with one of its hydrogen atoms either on γ- or α-oxygen on the surface and refill the vacancy in such a manner that two hydroxyl groups are formed. The energy gain is -1.83 and -1.61 eV, respectively. The dissociation can be accompanied by either cancellation or cancellation and creation of vacancies as indicated by the dashed lines which makes it difficult to formulate a reaction equation and predict the change in the resistance.

The calculations were additionally carried out for the vacancies on γ- and α-sites. The calculated dissociation energies and wavenumbers are shown in Table 3.5. The wavenumbers vary minimally with the previously (perfect surface and defective surface) calculated ones. They decrease slightly for the hydroxyl groups on the β- and the vacant oxygen site, and increase minimally for the hydroxyl groups on the γ-, δ- and α-sites.

The results gained here confirm, that SA has hydroxyl groups originating from the dissociation of water in the vacant oxygen sites and β-oxygen as well as from the dissociation in an oxygen vacancy and on a neighboring oxygen. A fourth and last situation should be considered, suggesting a hydroxylated surface with no vacancies where H_2O could dissociate.

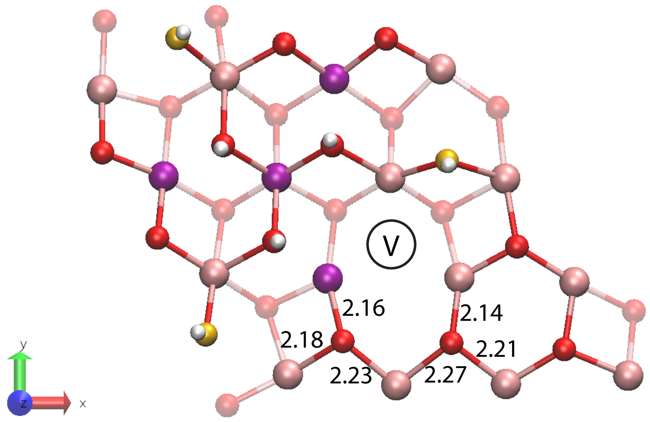

(a) Defect on δ-site.

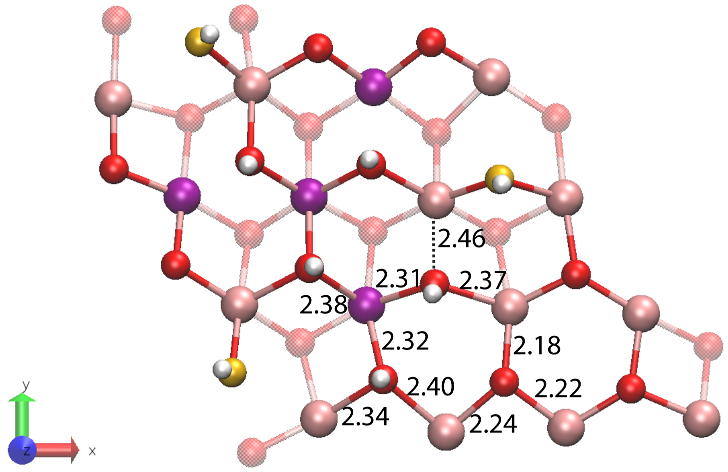

(b) Dissociated H_2O on δ and γ-site.

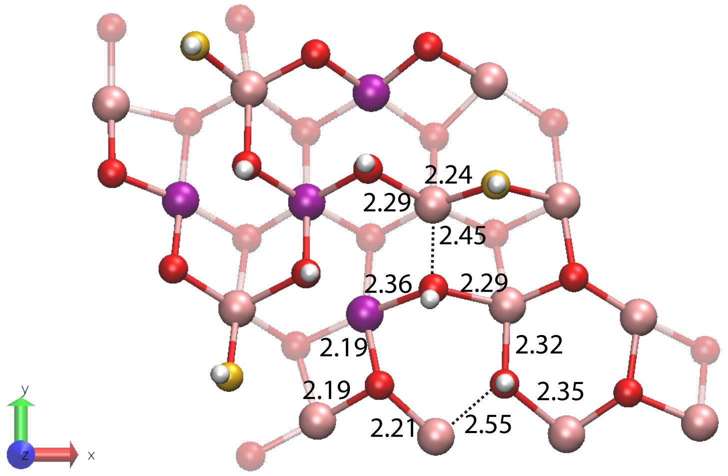

(c) Dissociated H_2O on δ and α-site.

Figure 3.17 Adsorption and dissociation of one H_2O molecule on $In_2O_3(111)$ hydroxylated and defective surface. Pink: In(5c), purple: In(6c), red: oop O, light red: ip O, yellow: oxygen from H_2O, white: H.

Table 3.5 Summary of the calculated dissociation energies and the wavenumbers of the hydroxylated defective In$_2$O$_3$(111). The wavenumbers of the last three calculations are not given since they are the same as the previous three.

Vacancy site	Adsorption site	ΔE [eV]	Surface species	Mode	$\tilde{\nu}$ [cm^{-1}]
δ	α-O	-1.83	O$_V$H	stretching	3751-3745
			O$_\beta$H	stretching	3721-3713
			O$_{V,\delta}$H	stretching	3679
			O$_\alpha$H	stretching	3648
			O$_V$H	bending	929
			O$_{V,\delta}$H	bending	907
	γ-O	-1.61	O$_V$H	stretching	3756-3742
			O$_\beta$H	stretching	3721-3707
			O$_{V,\delta}$H	stretching	3674
			O$_\gamma$H	stretching	3641
			O$_V$H	bending	1080, 920
			O$_{V,\delta}$H	bending	943
γ	α-O	-1.71	O$_V$H	stretching	3745-3741
			O$_\beta$H	stretching	3724-3711
			O$_\alpha$H	stretching	3652
			O$_{V,\gamma}$H	stretching	3648
			O$_V$H	bending	978, 937
	δ-O	-1.59			
α	δ-O	-1.91			
	γ-O	-1.81			

3.7.4 Adsorption and Dissociation on the Hydroxylated Surface

The last situation to be considered is a hydroxylated surface without vacancies. This is illustrated in Figure 3.18. The water molecule stays adsorbed on the surface without dissociating. H_2O positions itself in such a manner that hydroxyl bonds between the oxygen of the water molecule and the surface hydroxyl groups are formed with a length of 2.06 and 2.42 Å. One of the hydrogens of the water molecule and a surface oxygen also form a hydrogen bond with a length of 1.80 Å. The adsorption energy was calculated to be -0.57 eV and the calculated wavenumbers for the stretching mode are 3781, 3661, 3538, and 3197 cm^{-1} for the upper O-H of the water molecule, O$_\beta$H on the right, O$_\beta$H on the left and lower O-H group of the adsorbed water molecule, respectively.

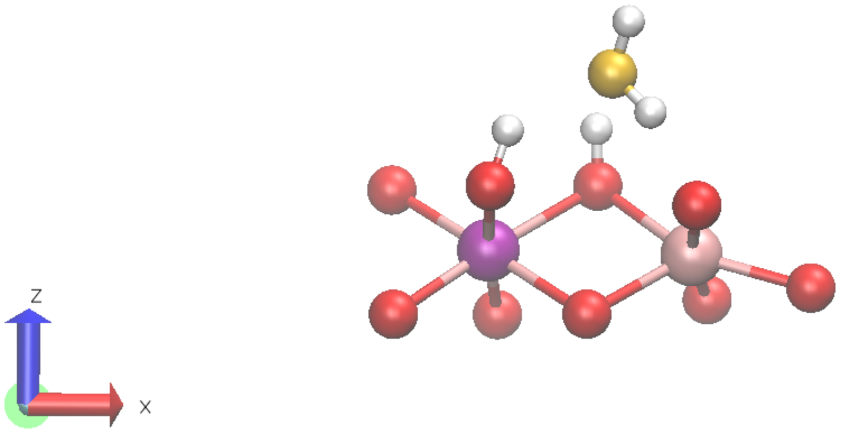

Figure 3.18 Adsorption of H_2O on a hydroxylated surface without vacancies.

Comparison of these results with the experimentally gained observations on IC1 and IC2 with the wavenumbers 3718, 3655, 3635, 3539, 3261 and 3720, 3655, 3637, 3570 3280 cm^{-1}, respectively, indicates, that already in dry syn. air a surface with hydroxyls and no vacancies is present. This shows that there is no place for H_2O to dissociate and thus is not able to change the sensor resistance, whereas SA has most probably a surface with defects making it possible for water molecules to adsorb and dissociate and consequently to change the sensor resistance.

It is important to note that, based on the DFT calculations, all hydroxyls on the surface of In_2O_3(111) are rooted ones which differ in their wavenumbers depending on the surface oxygen they occupy, which neighboring O-H groups they have and how many of them are present.

3.8 DFT Calculations of CO on In_2O_3(111)

CO is known to be a reducing gas with a very simple reaction mechanism. For SnO_2 and WO_3, it is known that it reacts with a lattice oxygen to form CO_2 and an oxygen vacancy releasing electrons back to the conduction band of the material [52, 62]. The DC resistance and DRIFTS measurements of the In_2O_3 sensors have shown, that their resistances under CO exposure in dry and humid air are quite similar and that the same In-O bands decrease when the materials are exposed to humidity and CO. This suggests that both molecules react with the same reaction partners on the surface of In_2O_3. Like in the case of SnO_2 and WO_3, DRIFTS measurements in nitrogen confirmed that for In_2O_3 also lattice oxygen is most probably the reaction partner of CO.

In order to confirm the assumptions and get further information on how the reaction takes place on the surface of In_2O_3, DFT calculations were performed. Again, a perfect $In_2O_3(111)$ surface is considered as the starting point.

3.8.1 Reaction on the Stoichiometric Surface

At the beginning, CO and the surface of In_2O_3 are considered to have no interaction. In the next step, CO places itself on the surface above a lattice oxygen. Since it was shown that different lattice oxygen species are present on the surface of In_2O_3, CO was positioned above β-, γ-, δ- and α-oxygen. Depending on the position, the adsorption energies vary between -0.03 for adsorption on the β-site and -0.07 eV for the adsorption above δ-oxygen. Since the adsorption on δ-oxygen is preferred, the adsorbed CO molecule on this position was pushed closer to the lattice oxygen to form a bond between the C of CO and lattice O. This resulted in the reaction of CO with the lattice oxygen, and the subsequent release of CO_2 with an energy gain of -1.06 eV.

For this specific case, the activation barrier was estimated with the drag method. Here the system is relaxed while keeping one coordinate, in this case the z-coordinate, fixed along the reaction pathway with a step size of 0.1 Å. The remaining x and y-coordinates were allowed to relax. The maximum energy is defined as the activation barrier. The reaction pathway is shown in Figure 3.19.

It was calculated that the CO molecule adsorbs first on an In-atom

$$\mathrm{CO_{gas}} + \mathrm{In_{In}} \longrightarrow \mathrm{In_{In}{-}CO_{ads}} \tag{3.7}$$

with an energy gain of -0.12 eV and an activation barrier of 0.22 eV before it reacts with the lattice oxygen. The activation barrier for the reaction of CO to CO_2 with O_O was found to be 0.40 eV accompanied with the creation of a vacancy. Also here, the corresponding wavenumbers were calculated, they were found to be 2090 and 2334 cm^{-1} for the adsorption of CO above the surface and after the reaction to CO_2, respectively. Based on the experiment results from the DC resistance and DRIFTS measurements in the context of the calculations, the following reaction

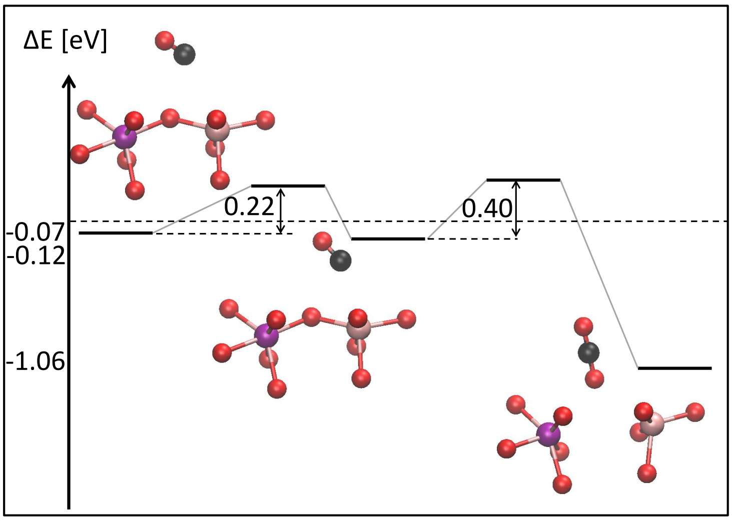

Figure 3.19 Energetic pathway of the adsorption and reaction of CO on the clean In$_2$O$_3$(111) surface. The CO molecule without interaction with the surface is considered as the zero reference energy.

is suggested:

$$\mathrm{CO_{gas}} + \mathrm{O_O} \longrightarrow \mathrm{CO_2} + \mathrm{V_O}^{++} + 2\,\mathrm{e}^- \tag{3.8}$$

showing that CO reacts with a lattice oxygen to form a vacancy, thus decreasing the resistance. This is the same oxygen that would also react with water to form a hydroxyl group.

The calculated wavenumber for CO$_2$ matches the experimentally observed value. The calculated wavenumber for adsorbed CO could not be observed in the DRIFTS. Presumably, the step from adsorption of CO to the reaction of it with lattice oxygen happens too fast to be observable in the DRIFTS. The observed wavenumbers for the carbon related surface species of IC1 and IC2 could not yet be identified using the calculations.

3.8.2 Reaction on the Defective Surface

Also here, four different defective situations were considered by removing β-, γ-, δ- and α-oxygen. The adsorption energies of CO for the vacancies at the β-, γ-, δ- and α-sites are -0.05, -0.03, -0.10 and -0.04 eV, respectively. Since the adsorption above the vacancy at the δ-site is preferred, the next reaction steps were made with this initial situation. The reaction pathway is shown in Figure 3.20. CO was placed near the vacancy causing the molecule to absorb with its C into the vacancy. In the following step, the adsorbed CO was forced to react with the nearest

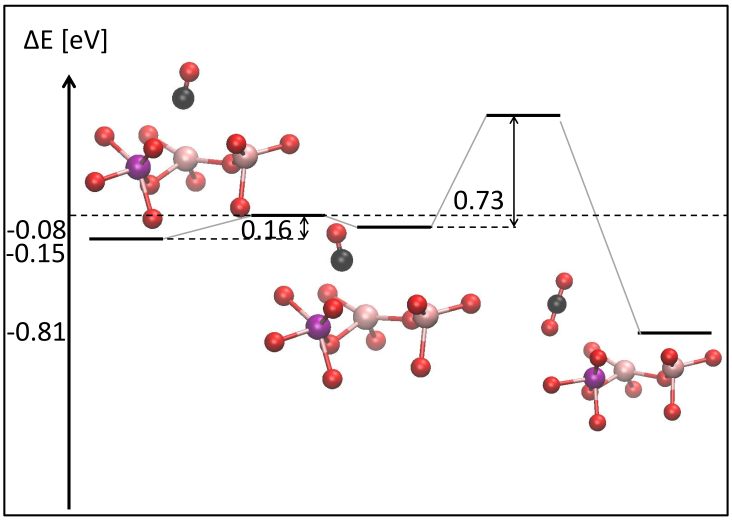

Figure 3.20 Energetic pathway of the adsorption and reaction of CO on the defective $In_2O_3(111)$ surface. The CO molecule without interaction with the surface is considered as the zero reference energy.

surface oxygen which was a β-oxygen to form CO_2. For this, the drag method in -x direction was used. First, this led to the adsorption of CO above In(6c) with an energy gain of -0.08 eV and an activation barrier of 0.16 eV. The reaction of CO with the lattice oxygen is accompanied by an energy gain of -0.81 eV which requires an activation barrier of 0.73 eV.

On the clean $In_2O_3(111)$ surface, the energy gain was higher with -0.12 and -1.06 eV for the adsorption and reaction of CO, respectively. Also, the calculated activation barrier was much lower (0.43 eV vs. 0.76 eV) for the reaction of CO with O_O. This indicates that the whole process is more favorable on the perfect surface than on a defective one. The reaction equations written for the perfect surface (Eq. 3.7 and 3.8), however, also apply for a defective surface.

The calculated wavenumbers are 2104 and 2337 cm^{-1} for the adsorption of CO and reaction to CO_2, respectively. They are quite similar to the ones calculated for the clean $In_2O_3(111)$. Also here, wavenumbers of carbon related species, which were observable for IC1 and IC2, could not be found.

3.8.3 Reaction on the Hydroxylated Surface

In this work, the effect of humidity on CO sensing was studied by DC resistance and DRIFTS measurements. It was shown that the resistance under CO exposure for both dry and humid conditions was similar. Additionally, the IR-experiments revealed that the same In-O bands decrease under exposure of both analytes. In order to understand how the reaction of CO can still occur, despite the hydroxyl groups on the surface, a hydroxylated surface, shown in Figure 3.17(c), is considered as an initial state.

Placing CO above the surface leads to the positioning of it over a hydroxyl group with an energy gain of -0.08 eV. In order to force the reaction of CO with the surface, again the drag method in -z direction was used. It was observed that the CO molecule moves away from the hydroxyl groups to reach a clean surface adsorption site. This way CO reacts with unoccupied oop oxygen to a carbon related surface species (shown in Figure 3.22(c)) accompanied by an energy gain of -0.29 eV and an activation barrier of 0.55 eV. This surface species can desorb as CO_2 creating an oxygen vacancy.

Calculating the wavenumber of this surface species reveals 1559 and 1057 cm^{-1}. They are significantly different from the observed ones (1480 and 1348 cm^{-1}) for IC1 and IC2 and are therefore unlikely to be present.

Comparison of the results gained in this section with the ones gained experimentally shows that as long as there are free oop oxygen atoms on the surface, the reaction of CO to CO_2 is not hindered. For SA, which probably has less hydroxyl groups on the surface in dry air, this means that CO can react with all available unoccupied surface oxygen atoms. As soon as humidity is introduced and some of the surface oxygen are changed to O-H groups, CO can only react with the remaining free oop oxygen. In other words, while a H_2O molecule needs adsorption sites and nearby vacancies for the formation of O-H groups, CO can react on the surface of In_2O_3 with lattice oxygen as long as it can adsorb on an In atom. Vacancies are not needed.

For IC1 and IC2 it is assumed that they are highly hydroxylated in dry air with no vacancies. As a result, the effect of humidity on the resistance is low and no additional significant hydroxylation takes place (no oxygen vacancies present). This would mean that CO reacts on both materials surfaces in dry and humid air with the same free oop oxygen since this oxygen cannot react into a hydroxyl group in humid air. Consequently, the relative change of the resistance of In_2O_3 under CO exposure in humidity is limited by the effect of water vapor.

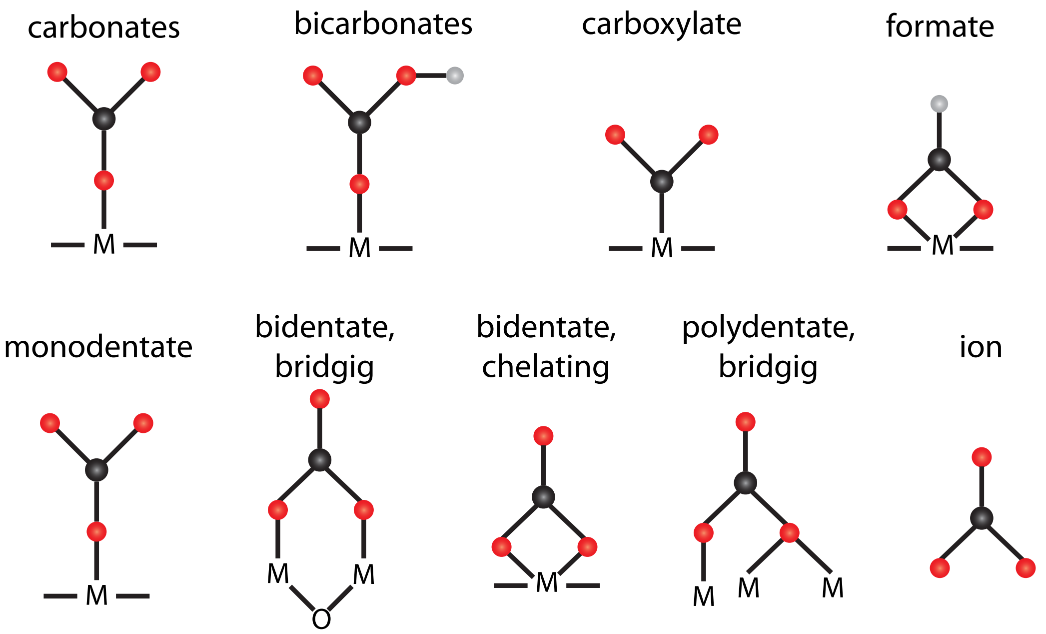

Figure 3.21 Adsorbed carbon related surface species. Black: carbon, red: oxygen, white: hydrogen. Adopted from [65, 66].

Based on the DRIFT spectra there seems to be a correlation between the formed carbon related surface species and the hydroxyl groups. Additionally, it has been shown that their formation is caused by a subsequent reaction of the formed CO_2. None of the wavenumbers calculated here for the adsorption and reaction of CO have matched with the experimentally gained results so far.

There are several possible surface carbon species, for example carbonate ($CO_3{}^-$), bicarbonate (CO_3H^-), carboxylate ($CO_2{}^-$) and formate ($HCO_2{}^-$) [65]. Additionally, there are different binding arrangements like monodentate, bidentate (chelating and bridging), polydentate (bridging) and as a free ion [66]. An illustration is shown in Figure 3.21.

Possible carbon related species with and without considering the participation of hydroxyl groups were formed on the surface of $In_2O_3(111)$. In order to determine which groups are present, the wavenumbers were calculated. The structures and the calculated wavenumbers are shown in Figure 3.22. Each structure shows at least two wavenumbers. They vary between 1748 and 1064 cm^{-1}. The comparison with the results gained from the DRIFTS experiments (1480 and 1345 cm^{-1}) show, that the structures in Figure 3.22(e) and 3.22(f) can be considered as possible species. Their wavenumbers are the closest to those determined experimentally.

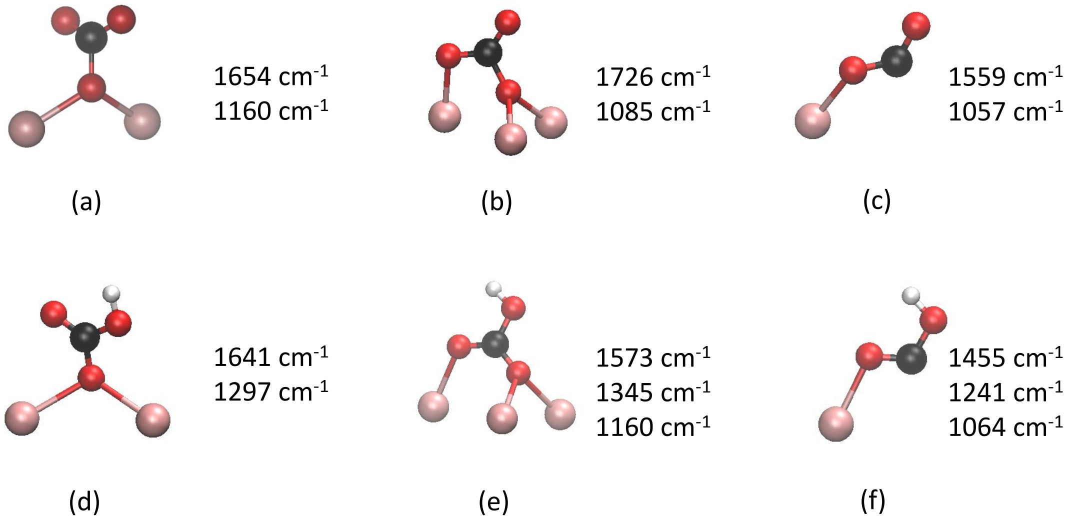

Figure 3.22 Possible carbon related species on the surface of In$_2$O$_3$(111).

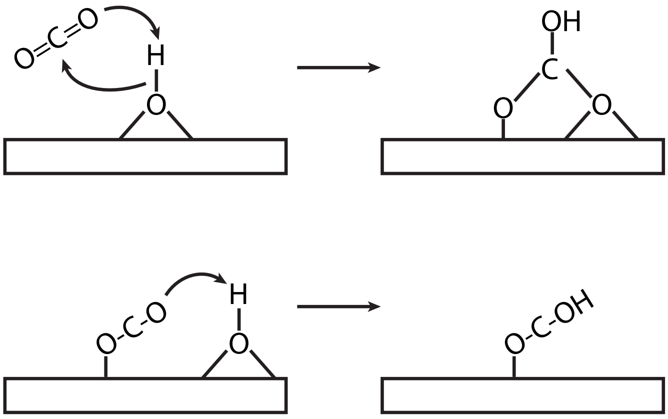

Figure 3.23 Proposed reaction mechanism for the formation of the surface species shown in Figure 3.22(e) and 3.22(f). In order for simplification, the Lewis structures were not considered.

Both structures have an O-H group confirming the assumption that for their formation a partially hydroxylated surface is needed.

Figure 3.23 shows one possible reaction mechanism for each structure. For the formation of the structure shown in Figure 3.22(e), a hydroxyl group on the surface is assumed where the hydrogen of the hydroxyl group adds to the oxygen of CO$_2$ which might simultaneously attack the oxygen of the hydroxyl group with its carbon forming a polydentate bicarbonate species. For the structure shown in Figure 3.22(f) a free metal adoption site is needed with a neighboring O-H group. After the adsorption of CO_2 on the surface, the hydrogen of the hydroxyl group can add to the formed structure.

3.9 Summary and Outlook of In_2O_3

Based on the results presented here it was possible to determine the surface reaction mechanism responsible for the response of In_2O_3 based gas sensors to water vapor and CO. The findings suggest that the way in which In_2O_3 is synthesized affects its surface termination and thus changes the electrical effect of water vapor dramatically.

SA shows less hydroxyl bands in the DRIFT spectra and at the same time shows a huge dependence of the resistance on the background humidity. This leads to the assumption that more hydroxyl groups can be formed in the presence of humidity. As a consequence, the resistance changes significantly.
IC1 and IC2 show more bands associated with hydroxyl groups, suggesting a high degree of initial hydroxylation in dry air. As a result the samples show low humidity dependence, as further hydroxylation is limited.

These assumptions were confirmed by DFT calculations which show that the wavenumbers vary because of the positions the hydroxyls take on the surface, the neighboring O-H groups and how many of them are formed. This means that the initial hydroxylation level of the three materials is different. The hydroxylation only takes place if unoccupied oxygen and a neighboring vacancy are present.

Based on the DFT calculations, in humidity, not all surface oxygen atoms can be hydroxylated, so there are still reaction partners left for reducing gases, in this case CO. This explains why its detection is not fully hindered. It was calculated that CO indeed reacts with lattice oxygen by adsorbing first on an indium atom and from there then reacting with an oop oxygen. This happens for the perfect as well as the defective surface. The hydroxylated surface shows that CO does not react with the hydroxyl groups, but tries to react with unoccupied oxygen.

Additionally, the DRIFTS measurements show the formation of carbonates which seems to be a subsequent reaction of formed CO_2. The effect of their formation on the resistance is, however, negligible. In humid conditions, their formation is significantly decreased. They are only observed for IC1 and IC2 suggesting that their formation is favored on highly hydroxylated surfaces. The DFT calculations suggest that not carbonates but bicarbonates could be the species which are observed in the IR-spectra.

Even though great efforts have been made in this chapter to explain the experimentally gained results, the picture is still incomplete. Further research regarding the role of water vapor with other analyte gases as well as the impact of temperature would be worthwhile. It was, however, possible to explain the humidity effect on the different materials and improve the understanding of In_2O_3. In the future it should be examined why In_2O_3 could have different levels of hydroxyls, how exactly the bicarbonates are formed, if the hydroxyl groups participate in the gas sensing reaction and how the operating temperature influences the resistance and sensing mechanism.

4

Effects of Rh- and Pt-Loading on In_2O_3

There are several ways to enhance the sensor properties, like selectivity, sensitivity and stability. One commonly used method is to add oxidized noble metal clusters to the surface [67–69]. Usually, commercially available gas sensors are not based on pure materials but on SMOX which contain some amount of a noble metal oxide. With more knowledge about the effects of the additives, noble metal oxides could be used in a more targeted manner.

For over three decades, the mechanism of surface loading has been widely researched. Yamazoe and Morrison were the first who proposed two fundamental mechanisms: the spillover and Fermi-level control mechanism. In the case of the spillover mechanism the surface loading activates the reaction between the analyte gas and the base material, whereas in the case of the Fermi-level control mechanism, the electrical properties of the additive are changed which changes the electrical coupling between both materials [68, 70].

Spectroscopic evidence was limited, but recently operando infrared studies have been published showing the Fermi-level control mechanism for WO_3 with oxidized Rh and Pt and SnO_2 with oxidized Pt [71–73]. This chapter will focus on the influence of oxidized Rh- and Pt-clusters loaded on In_2O_3 and how they change the sensor characteristics. In addition, it will be examined whether there are similarities between noble metal oxide loaded WO_3/SnO_2 and In_2O_3.

Major parts of the results shown in this chapter have already been published:

- R. Schnell, Eine Untersuchung von PtO_x geladenen In_2O_3 Gassensoren, Zulassungsarbeit, Eberhard Karls Universität Tübingen, **2019**.

- A. Staerz, I. Boehme, D. Degler, M. Bahri, D. E. Doronkin, A. Zimina, H. Brinkmann, S. Herrmann, B. Junker, O. Ersen, J.-D. Grunwaldt, U. Weimar, N. Barsan, Rhodium Oxide Surface-Loaded Gas Sensors, *Nanomaterials* **2018**, *8*(11), 892.
- 32^{nd} Eurosensors in Graz, Austria;
  I. Boehme, S. Herrmann, A. Staerz, H. Brinkmann, U. Weimar, N. Barsan, Understanding the sensing mechanism of Rh_2O_3 loaded In_2O_3.
  Corresponding article: I. Boehme, S. Herrmann, A. Staerz, H. Brinkmann, U. Weimar, N. Barsan, Understanding the sensing mechanism of Rh_2O_3 loaded In_2O_3, *Proceedings* **2018**, *2*, 754.
- S. Herrmann, Eine Untersuchung von Rh_2O_3 geladenen In_2O_3 Gassensoren, Zulassungsarbeit, Eberhard Karls Universität Tübingen, **2018**.

However, a considerable effort is made here to summarize the effects of noble metal loadings on In_2O_3 in a comprehensive manner.

4.1 Material Characterization

Loading In_2O_3 with noble metal clusters induces a change in color of the sensing layers. A picture of the sensors is shown in Figure 4.1.

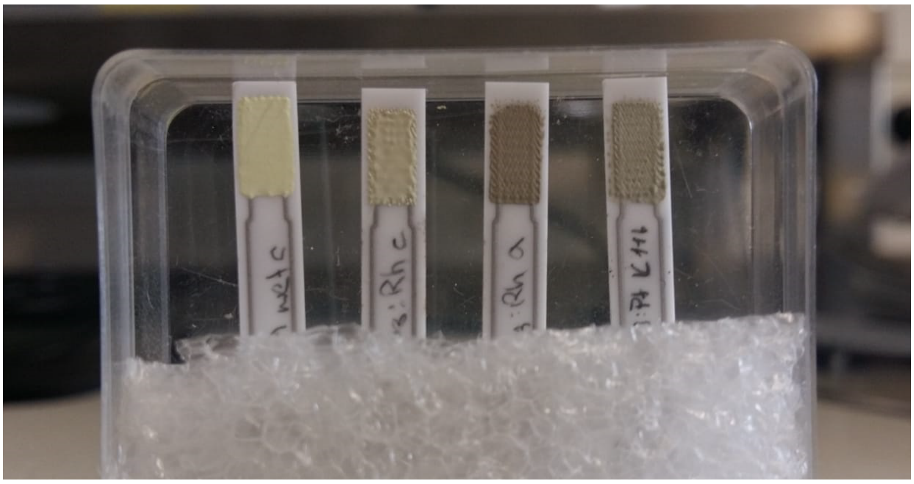

Figure 4.1 Picture of the sensors. From left to right: pure, 0.2 at% Rh-loaded, 1.0 at% Rh-loaded and 1.0 at% Pt-loaded In_2O_3.

With increasing amount of loading the color of the layer gets darker (compare 0.2 at% and 1.0 at% Rh-loaded In_2O_3). This observation was expected since the oxidized noble metal clusters are black [74].

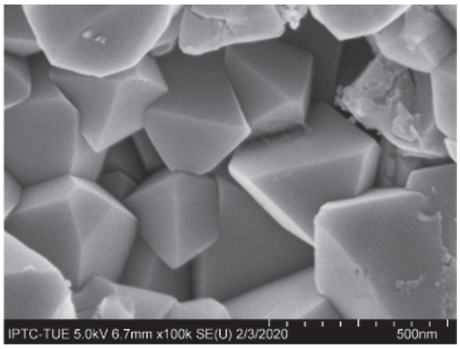

SEM image of pure In_2O_3.

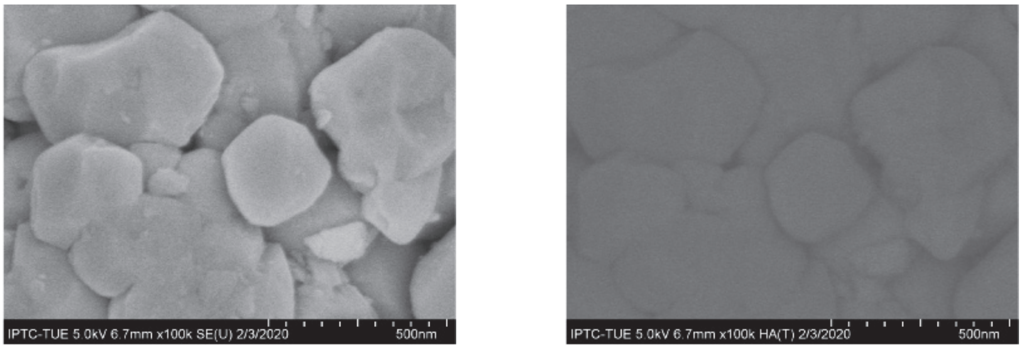

SEM image of 0.2 at% Rh-loading. BSE image of 0.2 at% Rh-loading.

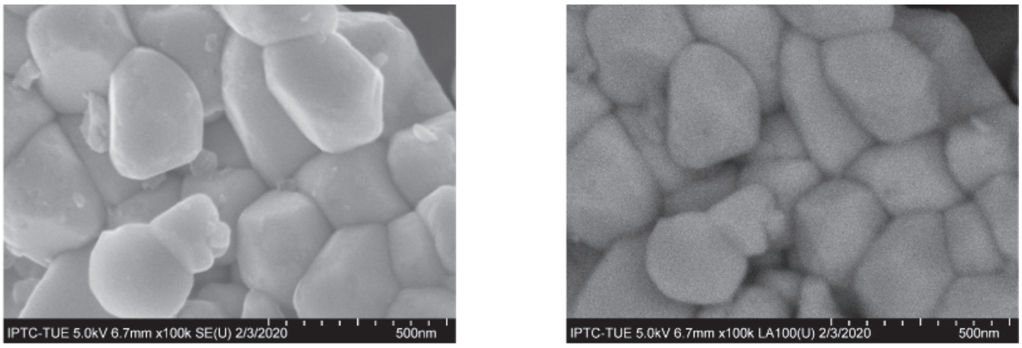

SEM image of 1.0 at% Rh-loading. BSE image of 1.0 at% Rh-loading.

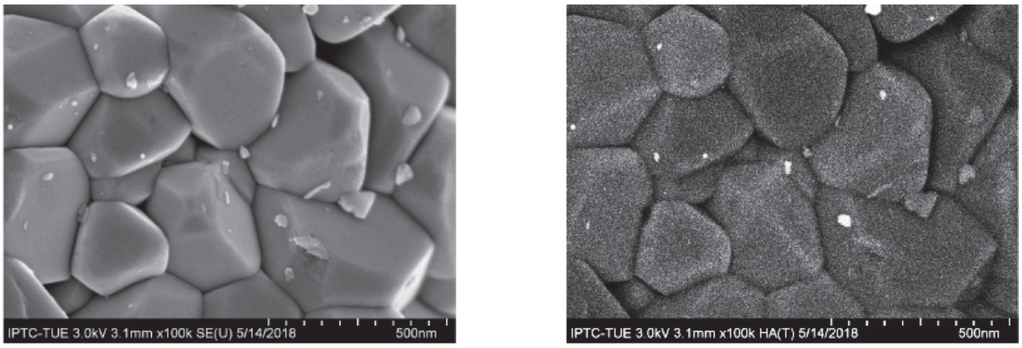

SEM image of 1.0 at% Pt-loading. BSE image of 1.0 at% Pt-loading.

Figure 4.2 On the left hand side SEM and on the right hand side BSE images of the sensitive layers at a magnification of 100,000x.

In attempt to extract further information, the materials were examined in the nano scale range by SEM and BSE. On the left in the SEM and on the right the BSE images at a magnification of 100,000x are shown in Figure 4.2. For the pure sample, an inhomogeneous particle size distribution is observable, ranging from 280 to 580 nm. Compared with the SEM results of SA, shown in section 3.1, the wet pretreatment does not affect the morphology of the material significantly. 0.2 at.% and 1.0 at% Rh-loaded In_2O_3 show similar SEM images, which are comparable with the unloaded material. Some smaller particles can be observed. From the SEM images, however, it is not obvious if these particles are In_2O_3 or result from the loading. From the same area, BSE images were taken for a mass-discrimination. It is considered that the higher the atomic number, the brighter the contrast. For In and Rh it is expected, that Rh should be shown as dark spots. In this case it is not possible to differentiate between the base material and the noble metal clusters. Two reasons can be given here: first, for 0.2 at% the amount of loading is probably not high enough and second, the difference in mass density between In (atomic number of 49 [74]) and Rh (atomic number of 45 [74]) is too low which makes it difficult to distinguish between these two elements. A distinction can be seen in the case of the Pt-loaded material. The Pt clusters (atomic number of 78 [74]), which are indicated by the brighter particles on the BSE image, can be separated from the In_2O_3 particles (darker particles) since the difference in mass seems to be sufficient enough for a discrimination. This shows the successful loading of the base material with platinum. The Pt-clusters are a few nanometers in size.

XPS measurements were carried out to identify the oxidation states of the additives. For the XPS measurements only 1.0 at% Rh- and 1.0 at% Pt-loaded In_2O_3 were used since the loading of 0.2 at% Rh-loading seems to be too low for any spectroscopic or microscopic measurements. The results are shown in Figure 4.3.

The fitted spectrum of the XPS measurement for the Rh-loaded sample (Figure 4.3 left hand side) exhibits a binding energy centered at 309.1 eV which can be assigned to the $Rh3d_{5/2}$ electron. According to the literature data (308.2 eV), this can be attributed to Rh(III), meaning that this noble metal is present as Rh_2O_3 [75–77]. Metallic rhodium would be expected at 307.2 eV [77]. The examined Pt-loaded sample (Figure 4.3 right hand side) shows binding energies for $Pt4f_{7/2}$ electrons to be at 71.3, 72.9 and 74.8 eV which are in good agreement

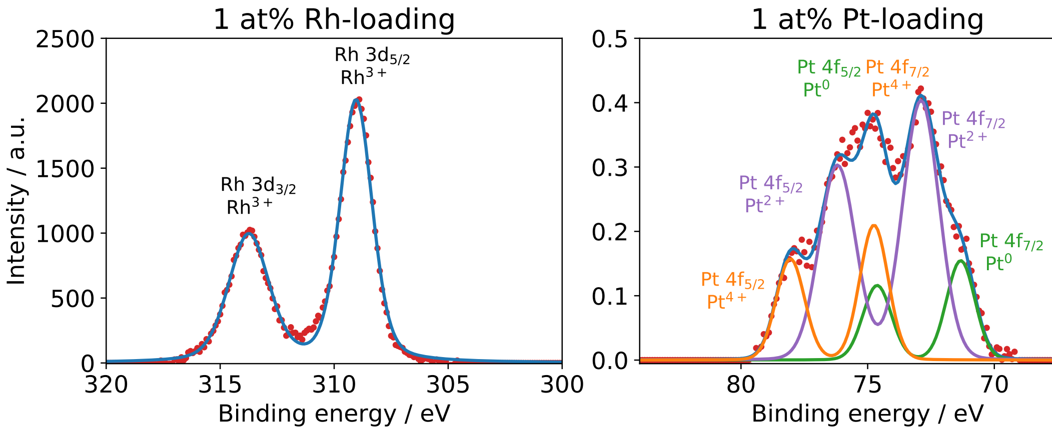

Figure 4.3 XPS measurements of 1.0 at% Rh and 1.0 at% Pt-loaded In_2O_3.

with metallic Pt, PtO and PtO_2, respectively [78, 79]. Since there is a mixture of different platinum species, this cluster will be denoted PtO_x.

4.2 Sensing Characteristics

4.2.1 DC Resistance Measurements

To understand how loading In_2O_3 with oxidized noble metal clusters influences the sensor characteristics, the sensors were exposed to various test gases in different humid conditions. For the detailed measurement conditions, see Table 5.1 in the Appendix. Even though samples loaded with oxidized noble metal clusters can be operated at low temperatures, the pure base material needs a higher operation temperature in order to show stable responses. For this reason, the DC resistance measurements were performed at 300 °C. For a direct comparison of the resistance changes, the raw resistance data of the unloaded and loaded samples are shown in Figure 4.4.

Loading changes the sensing characteristics dramatically. From the raw data, it is evident that adding oxidized Rh- and Pt- clusters results in an increase in the baseline resistance. This indicates an electronic interaction between the base material and the oxidized noble metal clusters. Additionally, the humidity dependence of the baseline resistance is considerably lower than for the pure material. While a 1 at% loading with rhodium shows no longer changes in the resistance, the 1 at% platinum loading still exhibits responses to the different target gases. Comparing 0.2 at% Rh- and 1.0 at% Pt-loading, they show similarities in the sensing characteristics. Additionally, a switch of the humidity dependence under exposure to

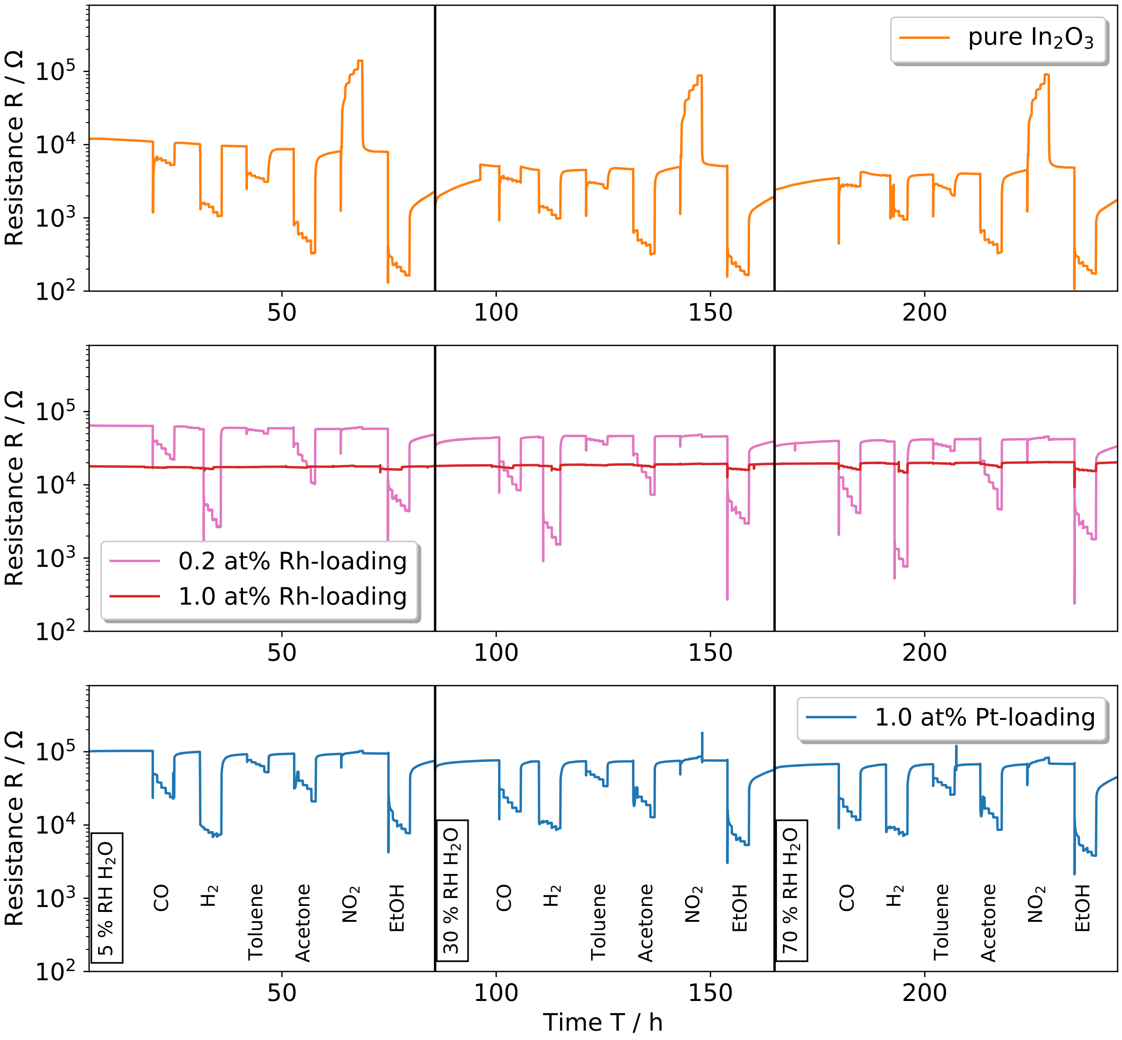

Figure 4.4 Resistance changes of pure, 0.2 at% Rh-loaded, 1.0 at% Rh-loaded and 1.0 at% Pt-loaded In$_2$O$_3$ under CO, H$_2$, toluene, acetone, NO$_2$ and ethanol exposure in 5, 30 and 70 % RH @ 25 °C and operation temperature of 300 °C.

analytes is observable for both 0.2 at% Rh-loading and 1.0 at% Pt-loading. They show an enhanced response to certain test gases in high humid backgrounds.

For a better comparison of the resistance changes and humidity dependencies, polar plots of the sensor signals were generated. Since 1.0 at% Rh-loading shows no resistance changes at all, it will be not taken into account in the polar plot evaluation. The plots are shown in Figure 4.5. It is apparent from the comparison of pure In$_2$O$_3$ and the loaded samples, that the disappearance of the NO$_2$ response is the most significant change, which is an inherent property of the pure sample [20–23]. This observation can be explained by two distinct hypotheses: firstly, Rh$_2$O$_3$ and PtO$_x$ are catalysts, which are known for the oxidation of NO to NO$_2$ [80,81]. This

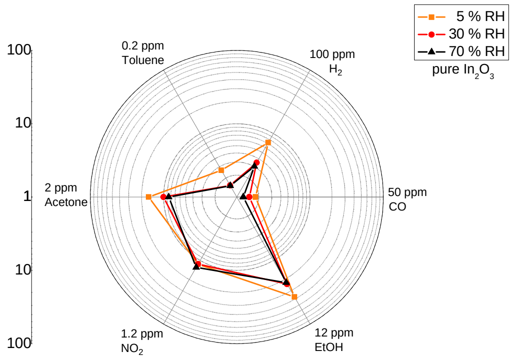

(a) pure In_2O_3

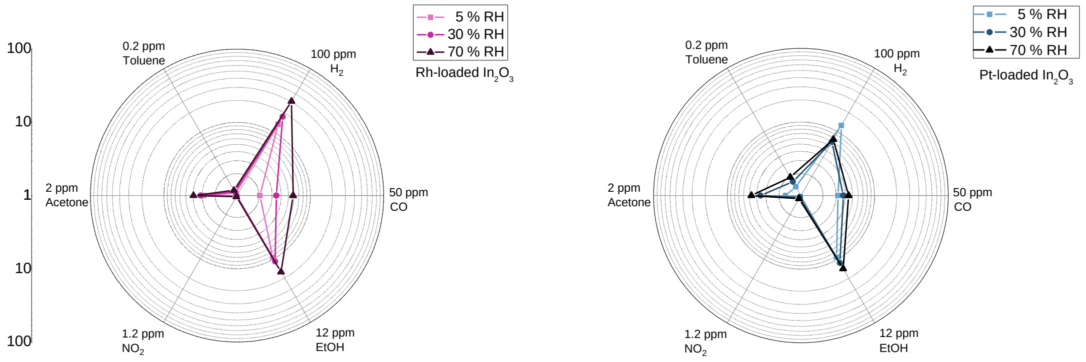

(b) 0.2 at% Rh-loaded In_2O_3 **(c)** 1.0 at% Pt-loaded In_2O_3

Figure 4.5 Polar plots with the sensor signals of the DC resistance measurements.

suggests that both noble metal oxides would be unsuitable sensing materials for the detection of NO_2. The second reason probably is that there are less electrons in the In_2O_3 particles due to a heterojunction-related depletion layer. This is caused by the loading (will be discussed in more detail in the next section) preventing the reaction of NO_2 on the surface of In_2O_3 as it is the case of Rh_2O_3 loaded WO_3 [72].

The response to CO and H_2 increases. Additionally, the switch of the humidity dependence is clearer for these two gases (except for 1 at% Pt-loading in 5 % RH): pure In_2O_3 shows a decrease of the signals under CO and H_2 exposure with increasing relative humidity, whereas the loaded samples show the opposite case. Rh and Pt are well-known catalysts for hydrogenation reactions and also for their ability to promote CO oxidation, making them ideal candidates for H_2 and CO detection [82–84].

The enhanced sensor signals under highly humid conditions suggest a water-involved sensing mechanism. Loading decreases the sensor signals for toluene and

Table 4.1 Results of the band bending calculation and the sensor signals.

Sensor	R_{N_2} / kΩ	$R_{syn.air}$ / kΩ	eV_β / meV	Sensor signal
pure In_2O_3	1.483	159.8	-	107
0.2 at% Rh-loading	46.96	1454.0	172	30.9
1.0 at% Rh-loading	40.46	96.23	165	2.37
1.0 at% Pt-loading	41.63	332.1	166	7.98

acetone dramatically. Also for ethanol, a decrease is observable. Still, for this VOC reasonable signals are shown and also in this case humidity enhances the sensor signal.

4.2.2 N_2-O_2 Measurements

The DC resistance measurements of the loaded samples already indicated an electronic interaction between the oxidized noble metal clusters and In_2O_3 by showing a higher baseline resistance compared to the pure sample. In nitrogen, the surface acceptor state associated without oxygen is assumed to be insignificant leading to a flat band situation for the pure material [85]. In this case only the presence of metal oxide clusters would lead to a band bending and thus to an increase of the resistance.

In order to examine the electronic coupling between the clusters and indium oxide, resistance measurements were carried out in N_2 at 300 °C. For this purpose, the sensors were kept in nitrogen until a stable baseline was reached and afterward exposed to dry syn. air. The measurements are shown in Figure 4.6.

A large increase of the resistance in nitrogen is observable. This suggests a strong electronic coupling between the oxidized noble metal clusters and indium oxide. Since in nitrogen the surface acceptor state caused by ionosorption of O_2 can be neglected, the band bending eV_β caused by oxidized noble metal clusters can be estimated using the following equation [73, 85]:

$$eV_\beta = kT \cdot \ln\left(\frac{R_{loaded,N_2}}{R_{pure,N_2}}\right) \tag{4.1}$$

where k is the Boltzmann constant, T the temperature, R_{loaded,N_2} the resistance of the loaded samples and R_{pure,N_2} the resistance of pure In_2O_3 in nitrogen. The results are shown in Table 4.1.

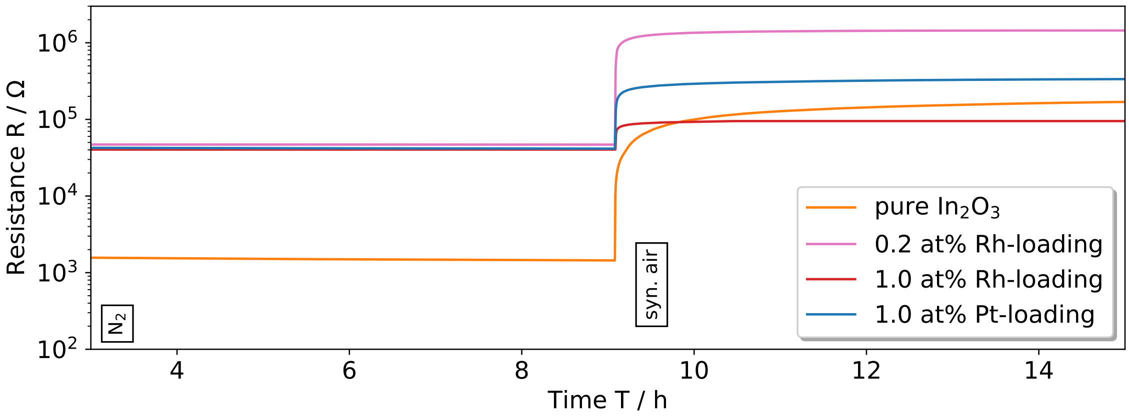

Figure 4.6 Sensor resistances in N_2 and syn.air at 300 °C.

All three loadings show similar initial band bending values of 172, 165 and 166 eV. The results indicate that a situation similar to that for Rh_2O_3 loaded WO_3 and PtO_x loaded SnO_2 can be assumed [72,86]: when the effect of the treatment during the synthesis on the band bending is considered negligible, showing a flat band situation (see Figure 4.7(a)), it can be concluded that the band bending of the loaded samples is caused only by the electrical coupling of the oxidized noble metal clusters with In_2O_3. The contact of the p-type Rh_2O_3 or PtO_x and n-type In_2O_3 leads to a p-n-heterojunction. Migration of electrons from indium oxide to Rh_2O_3/PtO_x takes place. The energy bands align and a depletion layer extends into In_2O_3. At the grain boundary the potential barrier gets larger (compare Figure 4.7(b)).

The change from N_2 to syn. air supports this assumption. This causes an increase of the resistances of all sensors due to the adsorption of oxygen with sensor signals of 107, 30.9, 2.37 and 7.98 for pure, 0.2 at% Rh-, 1.0 at% Rh- and 1.0 at% Pt-loading, respectively. Pure In_2O_3, however, shows the largest increase while the increase of the loaded samples is limited. An explanation is given by Staerz et al. and Degler et al. for Rh_2O_3 loaded WO_3 and PtO_x loaded SnO_2, respectively [72, 73], adapting here for Rh_2O_3 and PtO_x loaded In_2O_3: for the loaded samples in syn. air the adsorption of oxygen takes place on the surface of Rh_2O_3/PtO_x. This leads to an oxidation of the noble metal oxide clusters and thus to creation of more holes (see Figure 4.7(d)). This increases the work function of the noble metal clusters. Due to the increasing number of holes and change in work function, more electrons diffuse from the base material into Rh oxide/Pt oxide leading to an increase of the resistance. The electron deficit in the base material hinders the ionosorption of oxygen on the surface of In_2O_3. The change of the resistance of these materials is, however, limited and the oxidation of the pure material with atmospheric oxygen

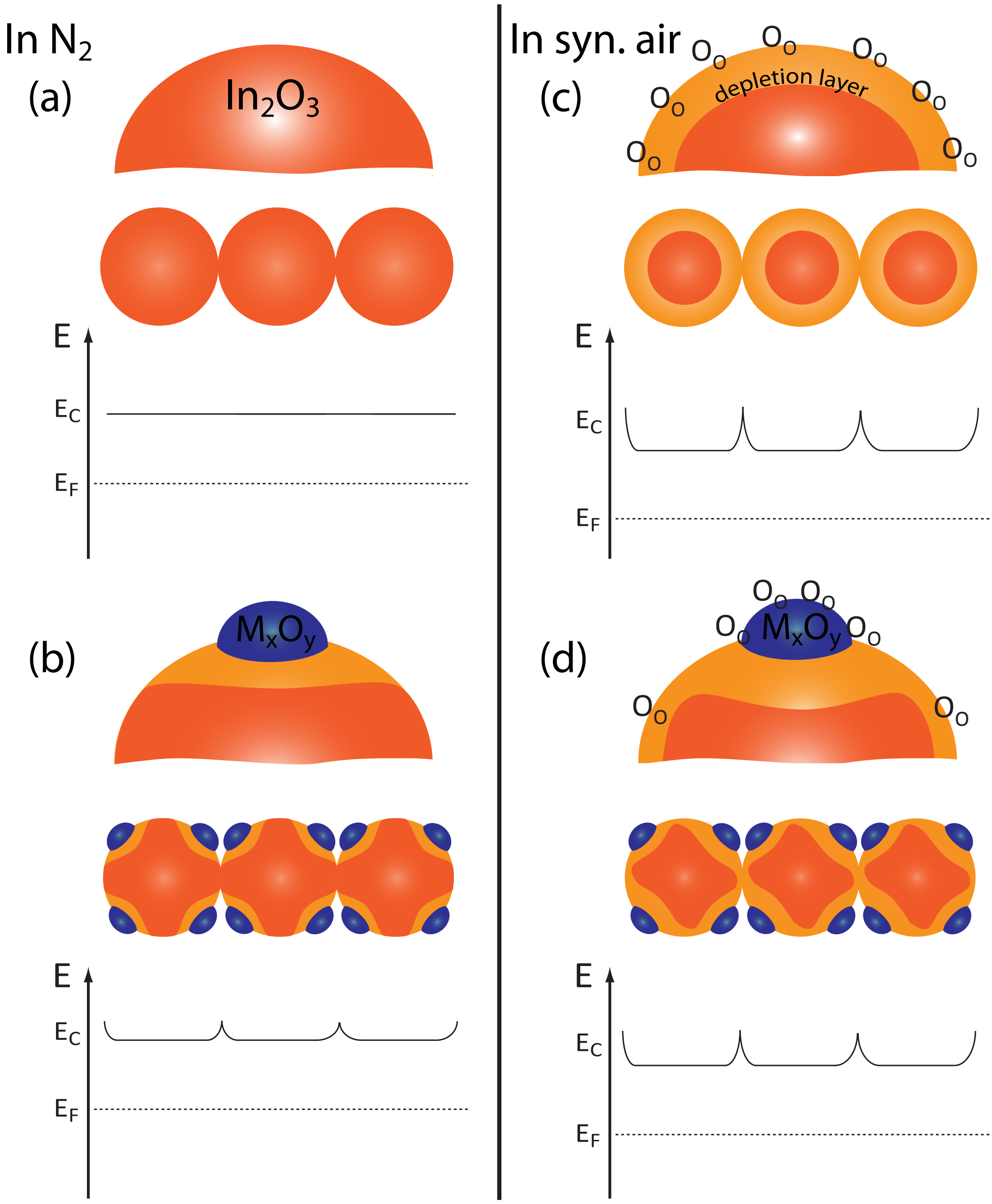

Figure 4.7 Surface of unloaded and Rh-/Pt-loaded In$_2$O$_3$ in nitrogen and syn. air. E$_C$: conduction band edge, E$_F$: Fermi-level. Adopted from [72].

seems to be more effective (Figure 4.7(c)). With increasing loading concentration (compare 0.2 at% and 1.0 at% Rh-loading), the effect of oxygen on the resistance of the higher loaded material, and thus the sensor signal, is lowered. Presumably, the size of the noble metal clusters increase with increasing loading amount. Hence, if the reaction takes place on the large noble metal clusters the change at the oxide-oxide interface, and thus the charge transfer between the cluster and the base material under O_2 exposure will be limited. This is probably also the reason why 1.0 at% Rh-loading showed no changes in the resistance under analyte gas exposure in the previous section.

4.3 DRIFT Spectroscopy Investigation

In order to verify the participation of the noble metal oxides during gas sensing, DRIFTS measurements are used [52, 72, 73]. Measurements were performed according to the procedure described in [73] which showed the examination of SnO_2 with oxidized Pt-clusters.

The sensors were operated at 300 °C and exposed to increasing CO concentrations (25 ppm, 50 ppm, 100 ppm, 200 ppm and 400 ppm) in N_2 with a low O_2 background (50 ppm). This way, the role of the surface clusters could be analyzed in more detail. Simultaneously, the DC resistance was recorded. Dividing the spectra gained under CO exposure by the spectrum gained under 50 ppm O_2 in N_2 provides revealing information. The DC resistance and the corresponding adsorption spectra are shown in Figure 4.8. For the exact flow protocol, see Appendix Table 5.2.

As expected, the resistance of pure In_2O_3 drops significantly for the first CO exposure and with increasing CO concentration the resistance decrease proceeds gradually showing a decrease in the sensitivity as a result of saturation. This is a well-known characteristic of SMOX based gas sensors [11, 87]. For 0.2 at% Rh-loaded In_2O_3, there is a huge drop in the resistance for the first concentration as well and, additionally, a significant decrease in the resistance from an oxygen rich condition (100 ppm CO) to an oxygen lean condition (200 ppm CO). This observation in the resistance is more pronounced for the higher loading concentrations 1.0 at% Rh-loaded and 1.0 at% Pt-loaded In_2O_3.

The simultaneously gained absorbance spectra indicate a change in the surface reaction which seems to be responsible for the change of the sensing characteristics. In the case of pure In_2O_3, exposure to CO results in a decrease of the In-O bands centered at 1537, 1274, 1102 and 1020 cm^{-1} for all CO concentrations. This shows the reduction of the surface of the material which is in line with the DC resistance measurements. The situation in the absorbance spectra is the same for 0.2 at% Rh-loaded. However, in the case of 1.0 at% Rh-loaded and 1.0 at%

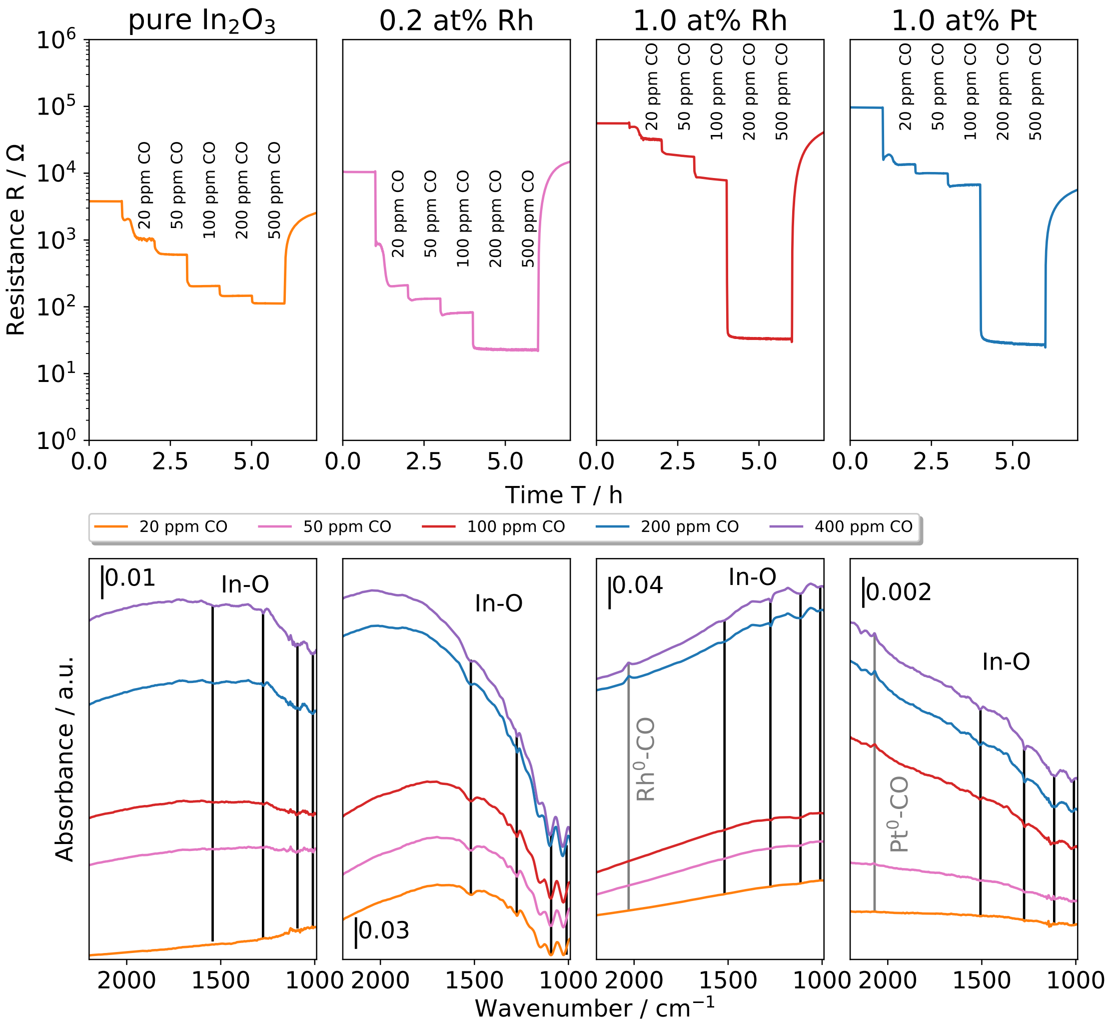

Figure 4.8 DC resistance measurements and the corresponding DRIFT spectra of pure, 0.2 at% Rh-loaded, 1.0 at% Rh-loaded and 1.0 at% Pt-loaded In_2O_3. The sensors were exposed to 25 ppm, 50 ppm, 100 ppm, 200 ppm and 400 ppm CO in nitrogen with 50 ppm O_2. The operation temperature was 300 °C. The spectra were referenced to nitrogen with 50 ppm O_2.

Pt-loaded In_2O_3 an interesting and unexpected observation can be made: under 20-100 ppm CO, there is little or no decrease of the In-O bands. As soon as an oxygen lean condition is reached, a significant drop in the resistance is detected and the decrease of the In-O bands becomes visible. Additionally, a band centered at 2028 cm^{-1} for 1.0 at% Rh-loaded and at 2069 cm^{-1} for 1.0 at% Pt-loaded In_2O_3 appears. These bands can be attributed to metallic rhodium carbonyl Rh-CO [88] and metallic platinum carbonyl Pt-CO [89], respectively.

In the 1980s, Yamazoe and Morrison proposed the spillover and Fermi-level pinning mechanism, which can be possible explanations for the surface reactions of loaded samples: the case of the spillover mechanism, the analyte molecule is adsorbed on the noble metal cluster. Consequently, the molecular bond of the analyte is weakened and the spillover of the adsorbate onto the surface of the base material takes place. The subsequent reaction occurs on the surface of the support material. In the case of the Fermi-level pinning, the noble metal cluster interacts with the SMOX base material. This contact leads to an alignment of both Fermi-level energies. The gas detection reaction takes place on the surface of the noble metal cluster. As a result, the electrical property of the noble metal cluster changes, hence changing the depletion layer and thus the resistance of the sensing layer as well [68, 70].

Recently, it has been reported that the Fermi-level pinning mechanism dominates the sensing mechanism of oxidized Rh- and Pt-loaded WO_3 and oxidized Pt-loaded SnO_2 [72, 73]. The results obtained in this chapter suggest the Fermi-level pinning mechanism for oxidized Rh- and Pt- loaded In_2O_3 as well. The DRIFT measurements have shown that the reaction between oxidized noble metal clusters and the target gases is the reason for the change in the sensing characteristics and the reaction initially dominates on the surface of the oxidized noble metal clusters (Figure 4.9(a)). Due to the CO exposure the Rh_2O_3/PtO_x clusters get reduced. By this interaction, the work function of the noble metal clusters change. Consequently, the depletion layer, which is caused by the contact between both materials, is affected which changes the resistance of the base material, see Figure 4.9(b). As long as there is enough O_2 in the background, the clusters get reoxidized. As soon as the concentration of CO increases and an oxygen lean condition is reached, which seems to be the case for $>$ 200 ppm CO for the Rh_2O_3 clusters and $>$ 100 ppm for PtO_x clusters, significant bands centered at 2028 and 2069 cm^{-1} appear which can be attributed to metallic rhodium carbonyl and platinum carbonyl, respectively. Under this condition, a reoxidation of the noble metal clusters cannot take place anymore and metallic rhodium/platinum is formed. At this point the resistance decreases significantly due to the formation of an accumulation layer and, presumably, a transition from p-n heterojunction to a metal-semiconductor junction takes place. Indicated by the decreasing In-O bands, the reaction moves to the surface of In_2O_3 at this point (Figure 4.9(c)).

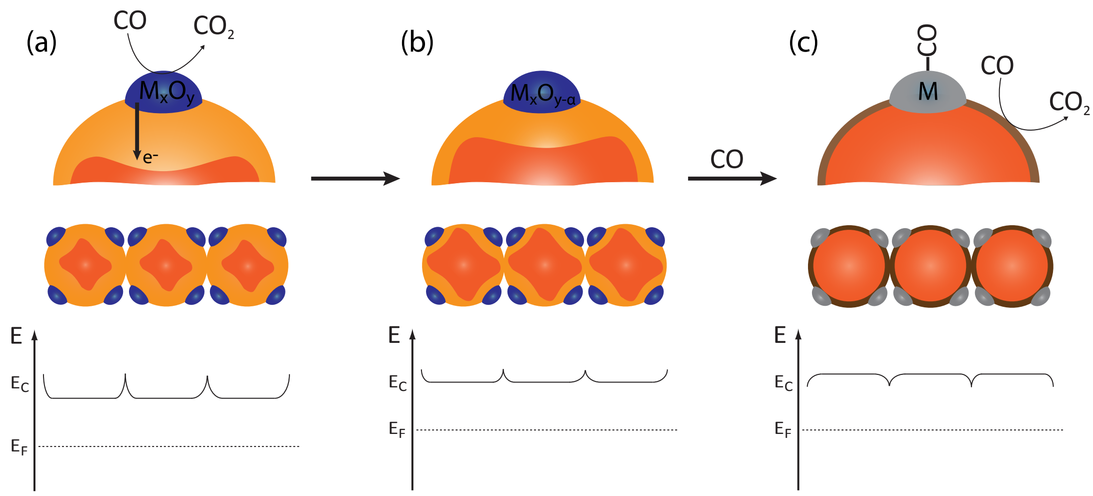

Figure 4.9 Surface of Rh- and Pt- laoded In$_2$O under exposure of CO in O$_2$ (a)/(b) rich and (b) lean condition. E$_C$: conduction band edge, E$_F$: Fermi-level. Adapted from [86].

4.4 Summary and Outlook of Loaded In$_2$O$_3$

In summary, loading In$_2$O$_3$ with oxidized noble metal clusters changes the sensing characteristics dramatically. None of the Rh and Pt-loaded samples responded to NO$_2$, which is an inherent property of In$_2$O$_3$. Also, the sensor signals for the VOCs decreased dramatically whereas the responses to CO and H$_2$ increased since both metals are known to be suitable catalysts for both target gases. The measurements in N$_2$ demonstrated that there is an electrical coupling between the noble metal clusters and the base material. The DRIFTS measurements succeeded in demonstrating that during gas sensing the reaction takes place on the noble metal clusters.

In total, these results suggest that the Fermi-level pinning mechanism dominates the sensing process. These findings add to a growing body of literature on loaded SMOX gas sensors and they are highly significant. The present results have important implications for solving the problem for the deliberate change of the sensing properties in a desired direction. Since the loading with Rh$_2$O$_3$ and PtO$_x$ show similar sensing characteristics, it does not seem to matter which of the two noble metals is used. They differ only in their amount of loading to show similar characteristics.

The present work has only investigated two noble metals. Consequently, further work needs to be done using other metals like Pd, Au or Ir. Also non-noble metals

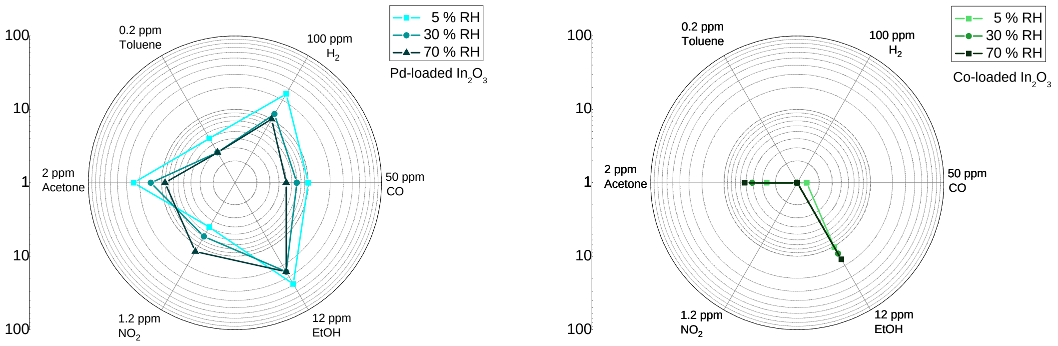

(a) 1 at% Pd-loaded In$_2$O$_3$. **(b)** 1 at% Co-loaded In$_2$O$_3$.

Figure 4.10 Polar plots of 1 at% Pd- and Co- loaded In$_2$O$_3$.

like Co, Ni or Fe are possible additives. Two exemplary measurements are shown in Figure 4.10 which demonstrate that Pd loading does not change the characteristics of the sensor, but enhances the sensor signals to all analyte gas whereas Co loading seems to change the properties of In$_2$O$_3$ in such a manner that the sensor gets selective to acetone and ethanol. There is a need to investigate whether the knowledge gained in this work can be transferred to other additives as well or if they show completely different sensing mechanisms.

5

Bibliography

---

[1] F. Reich, T.-H. Richter, *Journal für Praktische Chemie (in German)* **1863**, *90*, 172–176.

[2] S. Venetskii, *Metallurgist* **1971**, *15*, 148–150.

[3] A. F. Holleman, E. Wiberg, *Lehrbuch der anorganischen Chemie*, 102nd edition, Walter de Gruyter & Co., Berlin, **2007** .

[4] T. Minami, *Thin Solid Films* **2008**, *516*, 5822–5828.

[5] P. Prathap, A. S. Dahiya, M. Srivastava, S. K. Srivastava, B. Sivaiah, D. Haranath, Vandana, Ritu Srivastava, C. M. S. Rauthan, P. K. Singh, *Sol. Energy* **2014**, *106*, 143–222.

[6] L. S. Hung, C. H. Chen, *Mater. Sci. Eng. R Rep.* **2002**, *39*, 102–108.

[7] S. N. Malchenko, Y. N. Lychkovsky, M. V. Baykov, *Sens. Actuators B Chem.* **1993**, *13-14*, 159-161.

[8] W. H. Brattain, J. Bardeen, *Bell Telephone System Technical Publications Monograph* **1953**, 2086, 1-41.

[9] G. Heiland, *Z. Phys.* **1954**, *138*, 459-464.

[10] N. Taguchi, U.S. Patent 3,631,436, **1971**.

[11] N. Barsan, U. Weimar, *J. Electroceramics* **2001**, *7*, 143-167.

[12] N. Barsan, *Proceedings* **2019**, *14*, 53.

[13] D. R. Miller, S. A. Akbar, P. A. Morris, *Sens. Actuators B Chem.* **2014**, *204*, 250-272.

[14] C.-D. Kohl, T. Wagner, *Gas Sensing Fundamentals*, 1st edition, Springer, Berlin, **2014**.

[15] H. Yamaura, T. Jinkawa, J. Tamaki, K. Moriya, N. Miura, N. Yamazoe, *Sens. Actuators B Chem.* **1996**, *35-36*, 325–332.

[16] N. Singh, R. K. Gupta, P. S. Lee, *ACS Appl. Mater. Interfaces* **2011**, *3*, 2246–2252.

[17] N. M. Shaalan, M. Rashad, M. A. Abdel-Rahim, *Mater. Sci. Semicond. Process.* **2016**, *56*, 260–264.

[18] S. Elouali, L. G. Bloor, R. Binions, I. P. Parkin, C. J. Carmalt, J. A. Darr, *Langmuir* **2012**, *28*, 1879–1885.

[19] R. Xing, L. Xu, J. Song, C. Zhou, Q. Li, D. Liu, H. W. Song, *Sci. Rep.* **2015**, *5*, 10717.

[20] T. Takada, K. Suzuki, M. Nakane, *Sens. Actuators B Chem.* **1993**, *13-14*, 404-407.

[21] A. Gurlo, N. Bârsan, M. Ivanovskaya, U. Weimar, W. Göpel, *Sens. Actuators B Chem.* **1998**, *47*, 92-99.

[22] M. Ivanovskaya, A. Gurlo, P. Bogdanov, *Sens. Actuators B Chem.* **2001**, *77*, 264-267.

[23] J. Tamaki, C. Naruo, Y. Yamamoto, M. Matsuoka, *Sens. Actuators B Chem.* **2002**, *83*, 190-194.

[24] S. Wicker, M. Guiltat, U. Weimar, A. Hémeryck, N. Barsan, *J. Phys. Chem. C* **2017**, *121*, 25064-25073.

[25] D. Degler, *Sensors* **2018**, *18*, 3544.

[26] S. Sänze, A. Gurlo, C. Hess, *Angew. Chem. Int. Ed.* **2013**, *52*, 3607 –3610.

[27] S. Sänze, *Synthese, Charakterisierung und in situ spektroskopische Studie des Ethanol-Gassensormechanismus von Indiumoxid*, Technische Universität Darmstadt, **2014**.

[28] S. Roso, D. Degler, E. Llobet, N. Barsan, A. Urakawa, *ACS Sens.* **2017**, *2*, 1272-1277.

[29] N. Barsan, U. Weimar, *Fundamentals of Metal Oxide Gas Sensors*, 14th International Meeting on Chemical Sensors, **2012**.

[30] M. Wagner, P. Lackner, S. Seiler, A. Brunsch, R. Bliem, S. Gerhold, Z. Wang, J. Osiecki, K. Schulte, L. A. Boatner, M. Schmid, B. Meyer, U. Diebold, *ACS Nano* **2017**, *11*, 11531-11541.

[31] G. Chen, J. Li, *Green process Synth.* **2016**, *5*, 389-394.

[32] I. Can, *Investigation of Different* In_2O_3 *Base Material via DC Resistance Measurement and DRIFTS*, Eberhard Karls Universität Tübingen, **2017**.

[33] I. Can, U. Weimar, N. Barsan, *Proceedings* **2017**, *1*, 432.

[34] K.-I. Choi, S.-J. Hwang, ; Z. Dai, Y. Chan Kang, J.-H. Lee, *RSC Adv.* **2014**, *4*, 53130–53136.

[35] S. Herrmann, *Eine Untersuchung von* Rh_2O_3 *geladenen* In_2O_3 *Gassensoren*, Eberhard Karls Universität Tübingen, **2018**.

[36] R. Schnell, *Eine Untersuchung von* PtO_X *geladenen* In_2O_3 *Gassensoren*, Eberhard Karls Universität Tübingen, **2019**

[37] J. Kappler, *Characterisation of high-performance* SnO_2 *gas sensors for CO detection by in situ techniques*, Eberhard Karls Universität Tübingen, **2001**.

[38] S. Rank, *The Influence of the Electrode Material on the Sensor Characteristics of* SnO_2 *Thick Film Gas Sensors*, Eberhard Karls Universität Tübingen, **2014**.

[39] J. M. Olinger, P. R. Griffiths, *Anal. Chem.* **1988**, *60*, 2427-2428.

[40] `https://www.vasp.at/wiki/index.php/The_VASP_Manual` (accessed March 5, 2020).

[41] M. Wagner, J. Hofinger, M. Setvín, L. A. Boatner, M. Schmid, U. Diebold, *ACS Appl. Mater. Interfaces* **2018**, *10*, 14175-14182.

[42] W. Humphrey, A. Dalke, K. Schulten, J. Mol. Graph. **1996**, *14*, 33-38.

[43] H. Shang, C. Carbogno, P. Rinke, M. Scheffler, *Comput. Phys. Commun.* **2017**, *215*, 26-46.

[44] X. Wu, D. Vanderbilt, D. R. Hamann, *Phys. Rev. B* **2005**, *72*, 035105.

[45] G. Schaftenaar, J. H. Noordik, *J. Comput. Aided Mol. Des.* **2000**, *14*, 123-134.

[46] G. Schaftenaar, E. Vlieg, G. Vriend, *J. Comput. Aided Mol. Des.* **2017**, *31*, 789-800.

[47] M. Birkholz, *Thin Film Analysis by X-Ray Scattering*, Whiley-VCH, Weinheim, **2005**.

[48] A. Staerz, C. Berthold, T. Russ, S. Wicker, U. Weimar, N. Barsan, *Sens. Actuators B Chem.* **2016**, *237*, 54–58.

[49] S. Harbeck, A. Szatvanyi, N. Barsan, U. Weimar, V. Hoffmann, *Thin Solid Films* **2003**, *436*, 76-83.

[50] K. Großmann, R. G. Pavelko, N. Barsan, U. Weimar, *Sens. Actuators B Chem.* **2012**, *166-167*, 787-793.

[51] R. G. Pavelko, H. Daly, M. Hu, C. Hardacre, E. Llobet, *J. Phys. Chem. C* **2013**, *117*, 4158-4167.

[52] D. Degler, S. Wicker, U. Weimar, N. Barsan, *J. Phys. Chem. C* **2015**, *119*, 11792-11799.

[53] N. Yamazoe, J. Fuchigami, M. Kishikawa, T. Seiyama, *Surf. Sci.* **1979**, *86*, 335-344.

[54] H. D. Lutz, W. Eckers, H. Haeuseler, *J. Mol. Struct.* **1982**, *80*, 221-224.

[55] A. A. Tsyganenko, V. N. Filimonov, *J. Mol. Struct.* **1973**, *19*, 579-589.

[56] A. Walsh, C. Richard, A. Catlow, *J. Mater. Chem.* **2010**, *20*, 10438–10444.

[57] J. Ye, C. Liu, Q. Ge, *J. Phys. Chem. C* **2012**, *116*, 7817-7825.

[58] E. Balan, M. Lazzeri, G. Morin, F. Mauri, *Am. Mineral.* **2006**, *91*, 115–119.

[59] P. Djomgoue, D. Njopwouo, J. Surf. Eng. Mater. Adv. Technol. **2013**, *3*, 275–282.

[60] G. González-Gaitano, J. R. Isasi, *Chem. Educator* **2001**, *6*, 362–364.

[61] J. Baltrusaitis, J. H. Jensen, V. H. Grassian, *J. Phys. Chem. B* **2006**, *110*, 12005-12016.

[62] M. Hübner, M; C. E. Simion, A. Haensch, N. Barsan, U. Weimar, *Sens. Actuators B Chem.* **2010**, *151*, 103–106.

[63] G. Henkelman, H. Jónsson, *J. Chem. Phys.* **2000**, *113*, 9901-9904.

[64] G. Henkelman, H. Jónsson, *J. Chem. Phys.* **2000**, *113*, 9978-9985.

[65] G. N. Vayssilov, M. Mihaylov, P. S. Petkov, K. I. Hadjiivanov, K. M. Neyman, *J. Phys. Chem. C* **2011**, *115*, 23435–23454.

[66] C. Binet, M. Daturi, J.-C. Lavalley, *Catal. Today* **1999**, *50*, 207-225.

[67] N. Yamazoe, G. Sakai, K. Shimanoe, *Catal. Surv. from Asia* **2003**, *7*, 63-75.

[68] N. Yamazoe, Y. Kurokawa, T. Seiyama, *Sens. Actuators B Chem.* **1983**, *4*, 283–289.

[69] N. Yamazoe, *Sens. Actuators B Chem.* **1991**, *7*, 7-19.

[70] S. R. Morrison, *Sens. Actuators B Chem.* **1987**, *12*, 425-440.

[71] M. Anton, B. Buedy, *Sens. Actuators B Chem.* **1994**, *19*, 500–501.

[72] A. Staerz, A.; T.-H. Kim, J.-H. Lee, U. Weimar, N. Barsan, *J. Phys. Chem. C* **2017**, *121*, 24701–24706.

[73] D. Degler, S. A. Müller, D. E. Doronkin, D. Wang, J.-D. Grunwaldt, U. Weimar, N. Barsan, *J. Mater. Chem. A* **2018**, *6*, 2034.

[74] E. Riedel, C. Janiak, *Anorganische Chemie*, De Gruyter, Berlin, **2011**.

[75] A. Crucq, A. Frennet, *Catalysis and Automotive Pollution Control*, 1st edition, Elsevier, Amsterdam, **1987**.

[76] E. A. Derevyannikova, T. Y. Kardash, L. S. Kibis, E. M. Slavinskaya, V. A. Svetlichnyi, O. A. Stonkus, A. S. Ivanova, A. I. Boronin, *Phys. Chem. Chem. Phys.* **2017**, *19*, 31883.

[77] Y. Abe, K. Kato, M. Kawamura, K. Sasaki, *Surf. Sci. Spectra* **2001**, *8*, 117.

[78] Y. Abe, M. Kawamura, K. Sasaki, *Jpn. J. Appl. Phys.* **1999**, *38*, 2092-2096.

[79] E. Mazzotta, S. Rella, A. Turco, C. Malitesta, *RSC Adv.* **2015**, *5*, 83164.

[80] B. M. Weiss, N. Artioli, E. Iglesia, *ChemCatChem* **2012**, *4*, 1397–1404.

[81] K. Fujdala, T. Truex, J. Nicholas, J. Woo, *SAE International* **2008**.

[82] P. V. McKinney, *J. Am. Chem. Soc.* **1934**, *56*, 2577-2580.

[83] P. R. Watson, G. A. Somorjai, *J. Phys. Chem.* **1982**, *86*, 3993-3996.

[84] G. C. Bond, *Platinum Metals Rev.* **1957**, *1*, 88-93.

[85] N. Barsan, M. Hübner, U. Weimar, *Sens. Actuators B Chem.* **2011**, *157*, 510-517.

[86] D. Degler, Spectroscopic Insights in the Gas Detection Mechanism of Tin Dioxide Based Gas Sensors, Eberhard Karls Universität Tübingen, **2017**.

[87] J. Rebholz, P. Bonanati, U. Weimar, N. Barsan, *Anal. Bioanal. Chem.* **2014**, *406*, 3977-83.

[88] W. C. Hecker, P. B. Rasband, *J. Catal.* **1993**, *139*, 551–560.

[89] A. I. Serykha, O. P. Tkachenkoa, V. Y. Borovkova, V. B. Kazanskya, M. Benekeb, N. I. Jaeger, G. Schulz-Ekloff, *Phys. Chem. Chem. Phys.* **2000**, *2*, 5647-5652.

Appendix

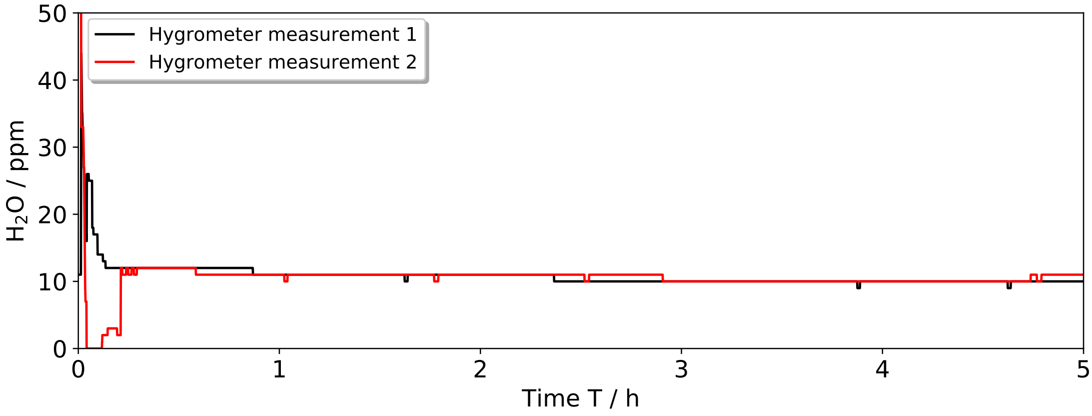

Figure 5.1 Hygrometer measurements of dry syn. air.

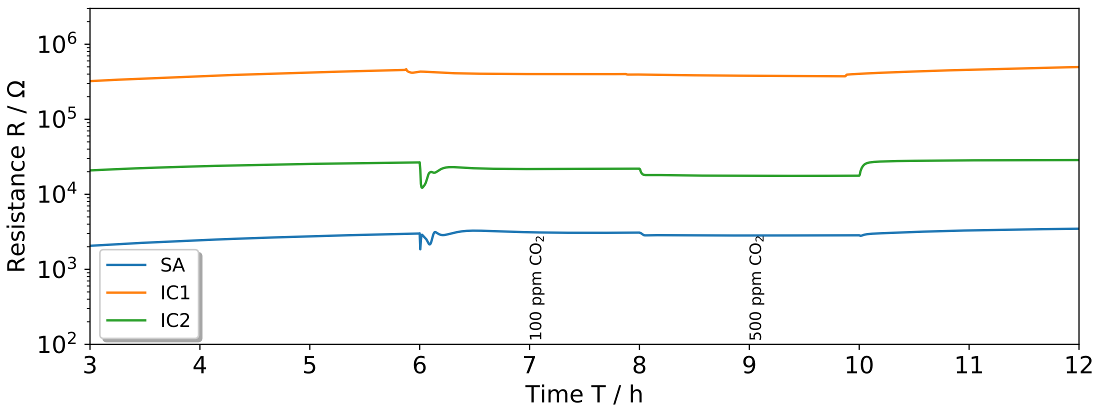

Figure 5.2 DC resistance measurments of SA, IC1 and IC2 under 100 and 500 ppm CO_2 exposure in dry syn. air at 300 °C.

Table 5.1 Flow protocol of the DC resistance measurment of pure, 0.2 at% Rh-loaded, 1.0 at% Rh-loaded and 1.0 at% Pt-loaded In_2O_3 in syn. air.

Duration [h]	RH [% @ RT]	Concentration [ppm]	Analyte
≥ 15	5/30/70		syn. air
5	5/30/70	20, 35, 50, 75, 100	CO
6	5/30/70		syn. air
5	5/30/70	70, 80, 100, 150, 200	H_2
6	5/30/70		syn. air
5	5/30/70	0.1, 0.15, 0.2, 0.25, 0.5	toluene
6	5/30/70		syn. air
5	5/30/70	0.75, 1.5, 2, 2.5, 5	acetone
6	5/30/70		syn. air
5	5/30/70	0.45, 0.8, 1.2, 1.5, 2.5	NO_2
6	5/30/70		syn. air
5	5/30/70	8, 10, 12, 14, 16	ethanol
≥ 6	5/30/70		syn. air

Table 5.2 Flow protocol of the in situ/operando DRIFTS measurments of pure, 0.2 at% Rh-loaded, 1.0 at% Rh-loaded and 1.0 at% Pt-loaded In_2O_3 in nitrogen.

Duration [h]	RH [% @ RT]	Concentration CO [ppm]	Concentration O_2 [ppm]
≥ 4	0	0	50
1	0	25	50
1	0	50	50
1	0	100	50
1	0	200	50
1	0	400	50
1	0	0	50

Publications

Full papers

- I. Boehme, U. Weimar, N. Barsan, Unraveling the Surface Chemistry of CO Sensing with In_2O_3 based Gas Sensors, *Sens. Actuators B Chem.* **2021**, *326*, 129004.

- T. Ueda, I. Boehme, T. Hyodo, Y. Shimizu, U. Weimar, N. Barsan, Au Loaded Porous-In_2O_3 Gas Sensors for Sensitive Detection of NO_2 at Lower Operating Temperatures, *Chemosensors* **2020**, *8*, 72.

- A. Staerz, I. Boehme, D. Degler, M. Bahri, D. E. Doronkin, A. Zimina, H. Brinkmann, S. Herrmann, B. Junker, O. Ersen, J.-D. Grunwaldt, U. Weimar, N. Barsan, Rhodium Oxide Surface-Loaded Gas Sensors, *Nanomaterials* **2018**, *8*(11), 892.

- T. Wang, I. Can, S. Zhang, J. He, P. Sun, F. Liu, G. Lu, Self-Assembly Template Driven 3D Inverse Opal Microspheres Functionalized with Catalyst Nanoparticles Enabling a Highly Efficient Chemical Sensing Platform, *ACS Appl. Mater. Interfaces* **2018**, *10*(6), 5835-5844.

- K. Vojisavljević, S. Wicker, I. Can, A. Benčana, N. Barsan, B. Maliča, Nanocrystalline cobalt-oxide powders by solution-combustion synthesis and their application in chemical sensors, *Adv. Powder Technol.* **2017**, *28*(4), 1118-1128.

Oral Presentations at Conferences

- 32nd Eurosensor in Graz, Austria;
  I. Boehme, S. Herrmann, A. Staerz, H. Brinkmann, U. Weimar, N. Barsan, Understanding the sensing mechanism of Rh_2O_3 loaded In_2O_3.

Corresponding article: I. Boehme, S. Herrmann, A. Staerz, H. Brinkmann, U. Weimar, N. Barsan, Understanding the sensing mechanism of Rh_2O_3 loaded In_2O_3, *Proceedings* **2018**, *2*, 754.

- 13th Sensor-Symposium in Dresden, Germany;
  I. Can, U. Weimar, N. Barsan, Operando-Untersuchung von In_2O_3-Sensoren durch kombinierte elektrische und optische Messungen.

- 3rd nanoFIS in Graz, Austria;
  I. Can, U. Weimar, N. Barsan, Investigation of H_2 exposure on In_2O_3 gas sensors in dry and humid air.

- 31st Eurosensor in Paris, France;
  I. Can, U. Weimar, N. Barsan, Operando investigations of differently prepared In_2O_3-gas sensors.
  Corresponding article: I. Can, U. Weimar, N. Barsan, Operando investigations of differently prepared In_2O_3-gas sensors, *Proceedings* **2017**, *1*, 432.

Academic Teachers

R. Anwander, N. Barsan, H. Bettinger, B. Casu, T. Chassé, R. Fink, G. Gauglitz, S. Grond, C. Huhn, M. Kramer, D. Kunz, M. E. Maier, H. A. Mayer, A. J. Meixner, H.-J. Meyer, B. Nachtsheim, U. Nagel, A. Oprea, H. Peisert, E. Schweda, P. Sirsch, U. Weimar, L. Wesemann, D. Wistuba, K.-P. Zeller, T. Ziegler

Danksagung

Erst durch die Unterstützung zahlreicher Menschen konnte ich meine Forschungsarbeit in eine schriftliche Form gießen, weswegen ich an der Stelle meine Dankbarkeit zum Ausdruck bringen möchte:

Mein Dank und meine Wertschätzung gilt an erster Stelle Herrn Dr. Nicolae Barsan, der mich während meiner Doktorarbeit unterstützt und betreut hat. Seine hilfreichen Anregungen und die konstruktive Kritik haben maßgeblich zum Entstehen und Gelingen der vorliegenden Arbeit beigetragen. Es war mir eine Freude, von seinem Fachwissen zu profitieren.

Bei Herrn Prof. Dr. Udo Weimar bedanke ich mich für die freundliche Aufnahme in seine multikulturelle Arbeitsgruppe sowie für die Bereitstellung des interessanten Dissertationsthemas.

Herrn Prof. Dr. Reinhold Fink danke ich für die Übernahme des Zweitgutachtens und zusammen mit Herrn Prof. Dr. Marcus Scheele und Herrn Prof. Dr. Holger Bettinger für die Bereitschaft, die Prüfungskommission bei der Verteidigung zu bilden.

Ein großes Dankeschön geht an Herrn Dr. Alexandru Oprea, der durch die technischen Umsetzungen diverser Versuche und Aufträge die Grundlage für die Messungen geschaffen hat.

Frau Dr. Anne Hemeryck von LAAS-CNRS danke ich für die Einführung in DFT und VASP sowie die Bereitstellung von Rechenzeiten.

Frau Elke Nadler von der Arbeitgruppe Chassé danke ich für die Aufnahmen der Bilder am Rasterelektronenmikroskop.

Auch möchte ich Benjamin Junker für die XPS-Messungen danken.

Ein Dankeschön geht auch an meine Bürokollegen für den Esprit im Büroalltag und die gute Arbeitsatmosphäre.

Weiter gilt mein Dank Dr. Anna Staerz, Tamara Ruß und Arne Kobald für das kritische Korrekturlesen.

Besonderer Dank kommt meinem Mann Martin zu für die bedingungslose Unterstützung und das wunderschöne Privatleben zusammen mit ihm und unserer Tochter Serra-Ida.

Schließlich gebührt meinen Eltern sowie meinen Schwestern Serenay und Ilayda besonderer Dank, die mich in all meinen Entscheidungen unterstützt haben und deren Geduld ich mehr als nur einmal auf die Probe gestellt habe.